Global variability of transition zone thickness

Yu J. Gu and Adam M. Dziewonski
Department of Earth and Planetary Sciences, Harvard University, Cambridge, Massachusetts, USA

Received 2 March 2001; revised 31 January 2002; accepted 5 February 2002; published 20 July 2002.

[1] We analyze recordings from more than 3000 shallow earthquakes and measure *S*410*S* – *S*660*S* differential travel times on a global scale. These differential times are obtained using a novel cross-correlation technique that eliminates effects associated with a priori assumptions of crustal thickness and velocity variations above the upper mantle transition zone. Our measurements show absolute perturbations up to 8 s from the global average (242 km), which imply transition zone thickness variations of ±20 km on a length scale of ~2000 km. The transition zone under major subduction zones, e.g., the western Pacific and South America, is significantly thicker than the global average; this could be associated with large-scale depressions of the 660-km discontinuity due to the accumulation of cold oceanic lithosphere at the base of the upper mantle. A narrow transition zone is observed under the central Pacific and northern Atlantic Oceans. We also observe a modest anticorrelation between *S*410*S* – *S*660*S* times and the delay times of shear waves (predicted using S12/WM13 [*Su et al.*, 1994]) in the transition zone, which suggests considerable thermal influence on the large-scale topography of the 410- and 660-km discontinuities. The lack of a stronger anticorrelation suggests that (1) compositional heterogeneities may be present and (2) a significant fraction of thermal anomalies near the transition zone do not extend through the transition zone and influence both the 410- and the 660-km discontinuities. A regional analysis shows that the transition zone is, on average, 6–8 km thicker under continents than under oceans; this implies a temperature difference of 50–70°C. However, we do not observe a clear correlation between thickness and the age of the crust. *INDEX TERMS:* 7218 Seismology: Lithosphere and upper mantle; 7203 Seismology: Body wave propagation; 8120 Tectonophysics: Dynamics of lithosphere and mantle—general; 8121 Tectonophysics: Dynamics, convection currents and mantle plumes; 7207 Seismology: Core and mantle; *KEYWORDS:* *S*410*S*–*S*660*S* times, transition zone, *SS* precursors, subducted slabs

1. Introduction

[2] The upper mantle transition zone plays a key role in our understanding of the thermal, chemical, and dynamic processes in the mantle. This region is bounded by two prominent (generally believed to be global) seismic discontinuities near 410 and 660 km, within which strong velocity and density gradients [e.g., *Dziewonski and Anderson*, 1981], as well as one [*Shearer*, 1990, 1996] or more [*Deuss and Woodhouse*, 2001] modest velocity jumps have been documented. Results from mineral physics often suggest that the 410- and 660-km discontinuities are caused by pressure-induced phase transitions [e.g., *Ringwood*, 1975; *Jackson*, 1983] from α-olivine to β-phase and from γ-spinel to perovskite + magnesiowüstite, respectively. The depths at which these phase transitions occur are strongly temperature-dependent. The Clapeyron slope of the α-olivine to β-phase transition is positive [*Katsura and Ito*, 1989], which implies that the presence of a low- (or high-) temperature anomaly will cause a local uplift (or depression) of the 410-km discontinuity. The depth of the 660-km discontinuity is expected to behave in the opposite manner owing to a potentially negative Clapeyron slope of the postspinel transition [*Navrotsky*, 1980; *Ito and Takahashi*, 1989]. The net temperature effect suggests that the transition zone (TZ) becomes thinner at high temperatures and thicker at low temperatures, provided that (1) the thermal anomalies extend vertically across the TZ and influence both phase transitions and (2) the effect of compositional heterogeneities is negligible. Hence thickness can be used as an effective measure of the existence and vertical extent of thermal structures within the TZ.

[3] Significant progress has been made in recent years in characterizing the TZ discontinuities from the analysis of secondary reflected waves. The most frequently analyzed phase groups are the reverberations of near-vertical *S* waves within the TZ (*ScS* reverberations) [*Revenaugh and Jordan*, 1991; *Revenaugh and Sipkin*, 1994; *Katzman et al.*, 1998], *P'P'* precursors [*Benz and Vidale*, 1993; *Le Stunff et al.*, 1995; *Xu et al.*, 1998], and *SS* precursors [e.g., *Shearer and Masters*, 1992; *Shearer*, 1993; *Gossler and Kind*, 1996; *Lee and Grand*, 1996; *Gu et al.*, 1998; *Flanagan and Shearer*, 1998a]. *Revenaugh and Jordan* [1991] reported strong topography on the 410- and 660-km discontinuities that would suggest lateral TZ temperature variations on the order of ±200 K. *Shearer* [1993] analyzed delay times of *SS* precursors and reported variations of TZ thickness in excess of

0148-0227/02/2001JB000489$09.00

±20 km; this result is consistent with those of *Gu et al.* [1998] and *Flanagan and Shearer* [1998a], which provides strong evidence for the existence of high-amplitude, large-scale thermal variations in the TZ.

[4] Because of limited global coverage, secondary converted waves have mostly been used in regional studies of the TZ discontinuities. The best studied phase groups are the *P*-to-*S* conversions [e.g., *Petersen et al.*, 1993; *Bostock*, 1996; *Vinnik et al.*, 1996; *Shen et al.*, 1996, 1998; *Dueker and Sheehan*, 1997; *Li et al.*, 1998; *Gurrola and Minster*, 1998] and *S*-to-*P* conversions [*Richards and Wicks*, 1990; *Vidale and Benz*, 1992; *Yamazaki and Hirahara*, 1994; *Estabrook et al.*, 1994; *Niu and Kawakatsu*, 1995; *Castle and Creager*, 1998]. *Vidale and Benz* [1992] reported an average temperature difference of 300–400 K between subduction zone and normal mantle. Such rapid temperature variations in regions of strong lateral velocity gradient are supported by more recent studies, for example, near the Hawaiian hot spot [e.g., *Li et al.*, 2000a]. Some of the above studies reported small-scale variations on the order of ±20 km in TZ thickness [e.g., *Dueker and Sheehan*, 1997] or more [*Li et al.*, 2000b]. These estimates are compatible with those obtained using long-period reflected waves.

[5] Questions regarding the average TZ thickness and range of thickness variations were raised by *Chevrot et al.* [1999] using *P*-to-*S* conversions (also referred to as *Pds* phases), where a "flat" TZ (with variations <10 km) was reported. Regional differences up to 15 km in TZ thickness exist between the results of *Chevrot et al.* [1999] and results obtained using *SS* precursors. Also, the average TZ thickness obtained by the *Pds* phases differs from that obtained using *SS* precursors by 8 km or more. In spite of the differences in wave types, frequency content, data coverage, and measurement assumptions used by the two methods, such systematic departures warrant further investigations.

[6] This study introduces a novel approach to measure *S*410*S* – *S*660*S* differential times. These differential times provide robust global estimates of TZ thickness without the need to know the depths of the 410- and 660-km discontinuities, the crustal thickness, or the velocity structure above the TZ. The data set used in this study contains more high-quality, *SH* component records than those used in earlier studies of *SS* precursors. Our study is not aimed at the short-wavelength structure associated, for example, with the topography of the 660-km discontinuity in the immediate vicinity of subducted slabs [e.g., *Wicks and Richards*, 1993; *Flanagan and Shearer*, 1998b]. Instead, our main goal is to examine the large-scale thickness variations of the TZ and their implications for the thermal/chemical variations in the mantle.

[7] There is considerable evidence that the spectrum of lateral heterogeneity is "red," i.e., dominated by low-degree harmonics, especially in the upper mantle [e.g., *Masters et al.*, 1982; *Su et al.*, 1994; *Li and Romanowicz*, 1996; *Gu et al.*, 2001a]. This result suggests that a significant fraction of the thermal anomalies that influence the TZ discontinuities are of relatively large scale. This provides a motivation to use long-period waves in the analysis of TZ thickness. Our stacking approach actually aids such an undertaking since it acts as an effective averaging tool.

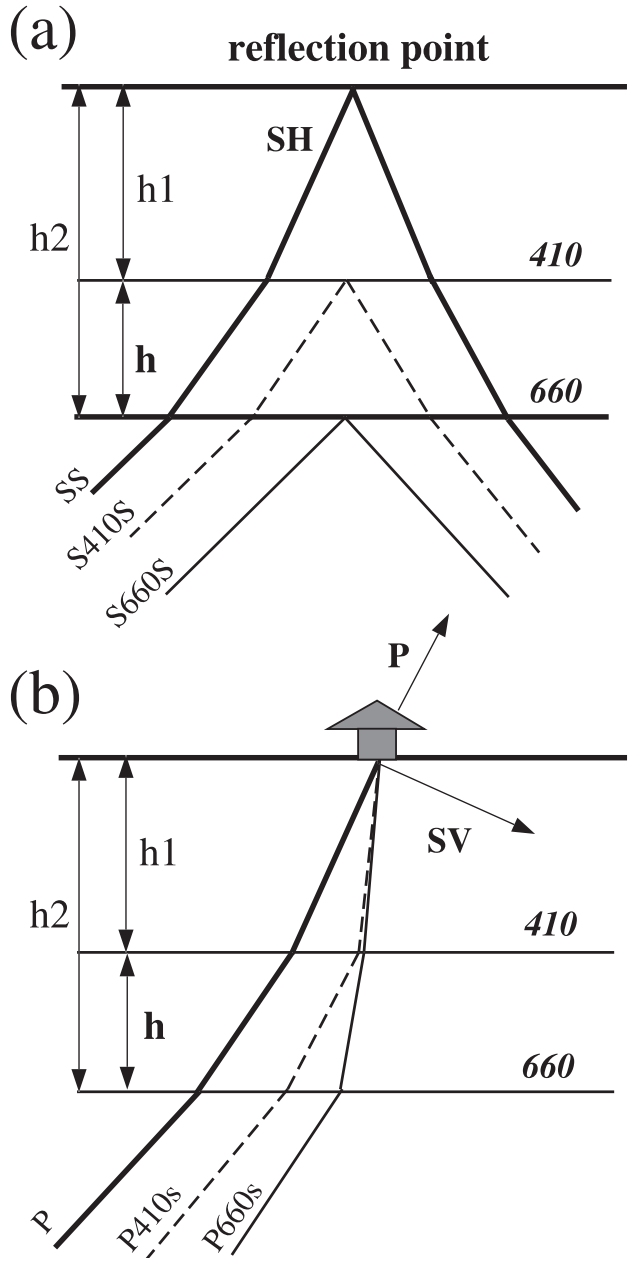

Figure 1. (a) A schematic ray diagram of *SS* and its precursors. This study infers the TZ thickness (*h*) from direct measurements of *S*410*S*–*S*660*S* (roughly twice the travel time of a near-vertical shear wave through the TZ). (b) A schematic ray diagram of *Pds* phases (*d* for a TZ discontinuity). TZ thickness (*h*) can be inferred from the differential times of (*P*660*s*–*P*)–(*P*410*s*–*P*) [e.g., CVM99], assuming the ray parameter and the *P* and *S* velocities in the upper mantle are known.

[8] For convenience, we will refer to the TZ discontinuities as the 410, 520, and 660, although their actual depths vary from region to region. Furthermore, we will hereinafter refer to *Gossler and Kind* [1996], *Gu et al.* [1998], *Flanagan and Shearer* [1998a], and *Chevrot et al.* [1999] as GK96, GDA98, FS98, and CVM99, respectively, in this study.

2. *SS* Precursors Versus *Pds* Phases

[9] The *SS* precursors are the most widely used phase groups in mapping the global TZ discontinuities, primarily because (1) their reflection points are not strictly limited by earthquake source or station locations and (2) their travel times offer significantly greater sensitivity for resolving the topography of mantle discontinuities than refracted waves. Figure 1a shows a schematic diagram of *SS* and its precursors *SdS* (*d* for a discontinuity) near the reflection points of the rays. Figure 1a is only for illustrative purposes, and the scale has been exaggerated for a better visual examination. Earlier studies [e.g., GDA98; FS98] obtained TZ thickness (*h*) by differencing *h2* (inferred from *SS*–*S*660*S*) and *h1* (inferred from *SS*–*S*410*S*). The differential travel times are measured on the *SH* component recordings, and the conversion from travel time to depth generally requires the assumptions of a ray parameter *p* and models of crust, surface topography, and the 3-D shear velocity of the upper mantle. Because this is an indirect measurement, errors in the analysis of either discontinuity (due to a lack of data coverage or complexities in the TZ) can potentially accumulate and affect the accuracy of TZ thickness. Therefore, instead of solving for the depths of the 410 and 660 (*h*1 and *h*2), this study exploits the similarity between the waveforms of *S*410*S* and *S*660*S* and measure their differential travel times directly using a cross-correlation technique. This approach essentially eliminates the potential errors associated with a priori assumptions of (1) mantle heterogeneities above the transition zone and (2) variations in crustal thickness and free-surface topography.

[10] In comparison, short-period *Pds* phases provide local constraints on TZ thickness under seismic stations. Following the significant increase in the number of seismic stations in recent years, it has become possible to use these phases to make inferences about the global characteristics of the TZ discontinuities. Figure 1b shows a schematic diagram of *P* and *Pds* waves beneath a seismic station. The *Pds* phases are compressional waves that convert to shear upon incidence at an upper mantle discontinuity *d*. By projecting arrays of teleseismic recordings on the *L* (or *P*), *H* (or *SV*), and *T* (or *SH*) axes, travel times of *Pds*–*P* can be obtained by subtracting the arrival times of *P* on the *L* axis from the corresponding *Pds* on the *H* axis [CVM99]. The conversion depths (*h1* and *h2*) can then be deduced from these differential times, assuming the ray parameter *p* and *P* and *S* velocities are known.

[11] There is a significant difference in the resolution of the *SdS* and *Pds* phases in their abilities to image TZ thickness. The quarter-period Fresnel zone (or the "footprint") that a 20-s *SdS* wave projects on the surface of a mantle discontinuity is a minimaximum pattern [e.g., *Shearer*, 1993; *Gu*, 2001] with an approximate width of 15–20°. This translates to a lateral dimension of 1500–2000 km, and thus small-scale topographic variations, e.g., in the vicinity of subduction zones or hot spots, are effectively averaged out or strongly attenuated. The resolution is further constrained to long wavelengths by the phase equalization approach (commonly referred to as "stacking"); the large size of the averaging caps (10°) imposes an effective low-pass filtering with corners at about ℓ = 10, or the half wavelength of ~2000 km. On the other hand, the half-period Fresnel zone of a 6-s *P*-to-*S* converted wave [e.g., CVM99] is nearly circular with a diameter of 200–300 km. This implies that most of the small-scale topography on the TZ discontinuities, e.g., imaged by *Pds*, has little influence on the travel times of the long-period *SS* precursors. Difference in the lateral resolution of these two types of phases could, and should in theory, account for some of the discrepancy between the results of CVM99 and those of *SS* precursors [e.g., FS98, GDA98]. More discussion of the potential sources of discrepancies between these results will be given in section 7.

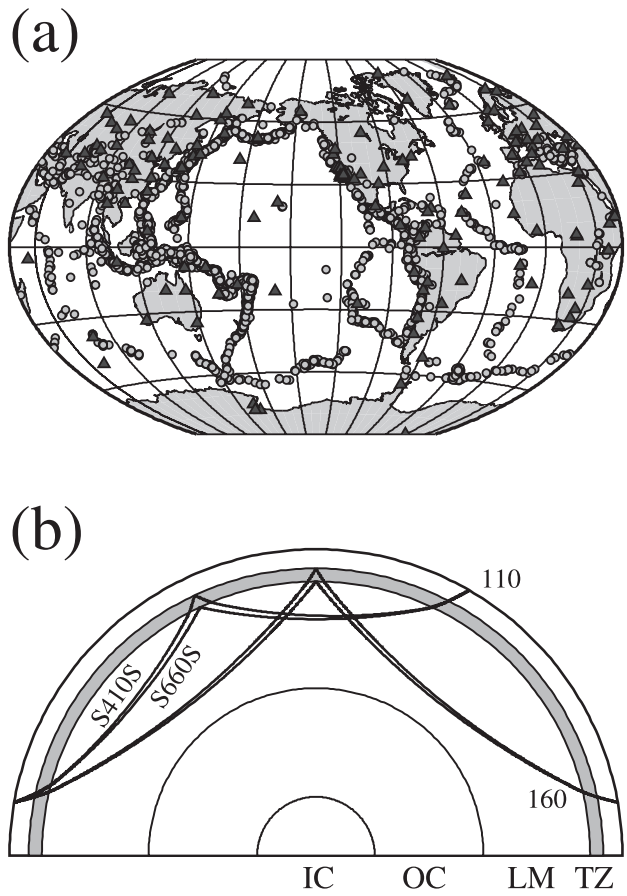

Figure 2. (a) More than 3000 shallow earthquakes (circle) and 130 stations (triangle) from GSN, Geoscope, MEDNET, and other seismic networks. This data set produces more than 19,000 high-quality, *SH* component records. (b) Underside reflections from the 410 and 660 at the distances of 110° and 160°. The travel times of *S*410*S*–*S*660*S* are primarily sensitive to the thickness of the TZ (shaded region) near the reflection points.

3. Data and Method

[12] Our data sets include recordings from Global Seismographic Network (GSN), Geoscope, Mediterranean seismographic network (MEDNET), and other seismic networks. Figure 2a shows the locations of more than 130

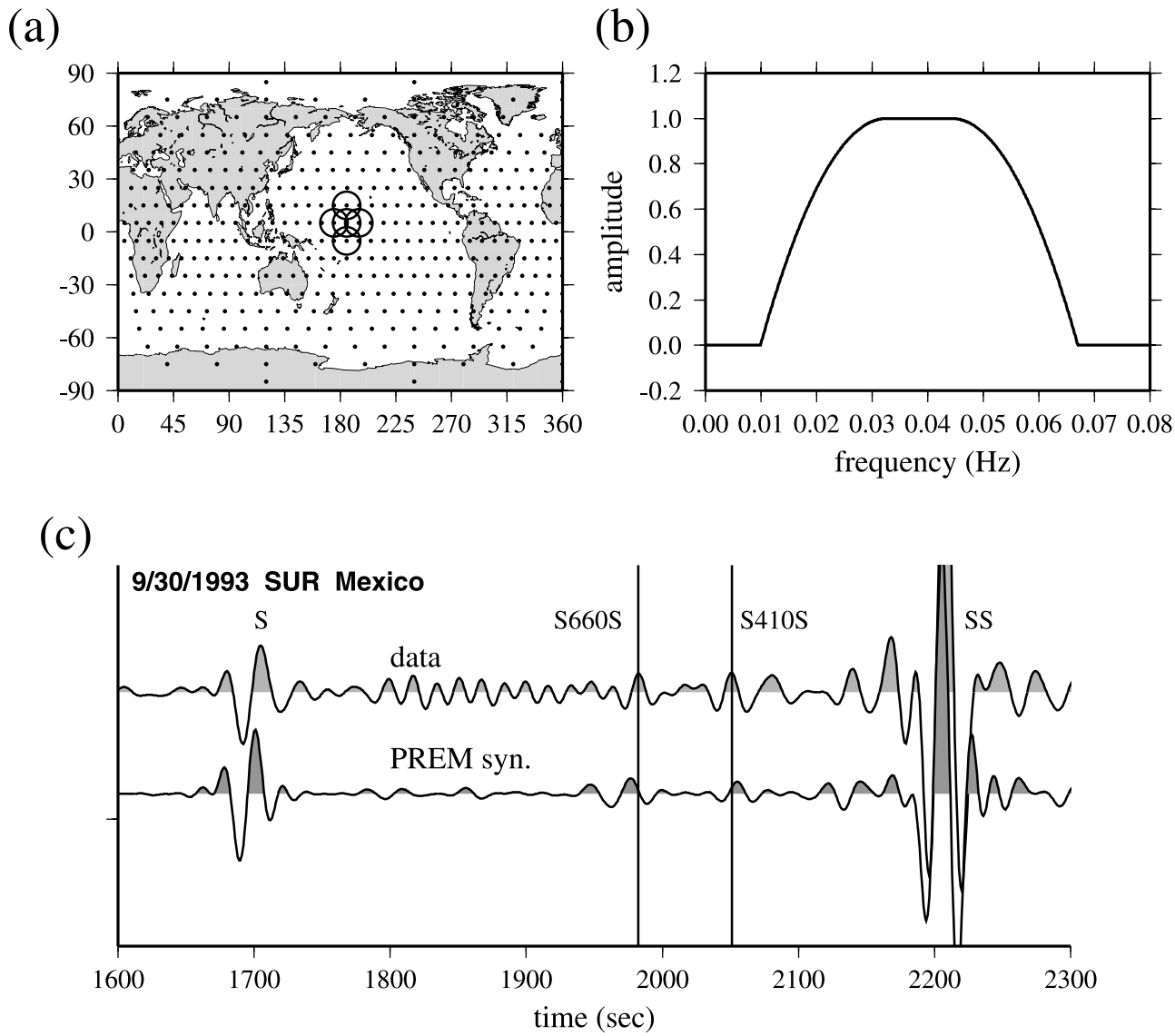

Figure 3. (a) Locations of 412 nearly equal-area, 10°-radius caps. The overlapping circles represent the effective averaging areas used in our stacking approach. (b) The Half-Welch filter that has been applied to the original long-period records. The cutoff periods (15 and 100 s) produce clear signals from the *SS* precursors. (c) A sample record (*SH* component) from an earthquake near the coast of Oaxaca, Mexico. Both the observed and PREM [*Dziewonski and Anderson*, 1981] synthetic seismograms show clear *S*, *S*660*S*, *S*410*S*, and *SS* arrivals. The observed differential travel time of *S*410*S* and *S*660*S* is approximately 11 s shorter than that predicted by PREM; this suggests the TZ is significantly narrower than 270 km (predicted by PREM) near the midpoint between the source and receiver.

stations and 3000 shallow earthquakes with source depths <75 km and $M_s \geq 5.5$. After automatic and interactive editing, we obtain ~19,000 high-quality *SH* component seismograms globally; this is ~45% and 70% more than those used in GDA98 and FS98, respectively, and nearly 3 times as much as that used in GK96 and *Deuss and Woodhouse* [2000] for a global analysis of *SS* precursors. Many of the new reflection points fall in previously undersampled regions such as South America, the southern Pacific, Atlantic and Indian Oceans, thus allowing us to resolve TZ thickness more reliably.

[13] Figure 2b shows two ray paths typical of selected data range (between 110° and 160°), calculated using Preliminary Reference Earthquake Model (PREM) [*Dziewonski and Anderson*, 1981]. These secondary reflections are particularly sensitive to the topographic variations of the 410 and 660 near the reflection points. Their travel time difference, which mainly results from the two-way *S* wave travel time within the TZ (shaded region), provides valuable information about the velocity structure and TZ thickness. The overlap of the ray paths near the Earth's surface essentially removes any effect associated with the velocity structure near the earthquake source and receiver.

[14] We use the stacking technique to enhance the signal-to-noise ratio of the secondary reflections. Ray paths are binned into 412 nearly equal-area spherical caps (10°

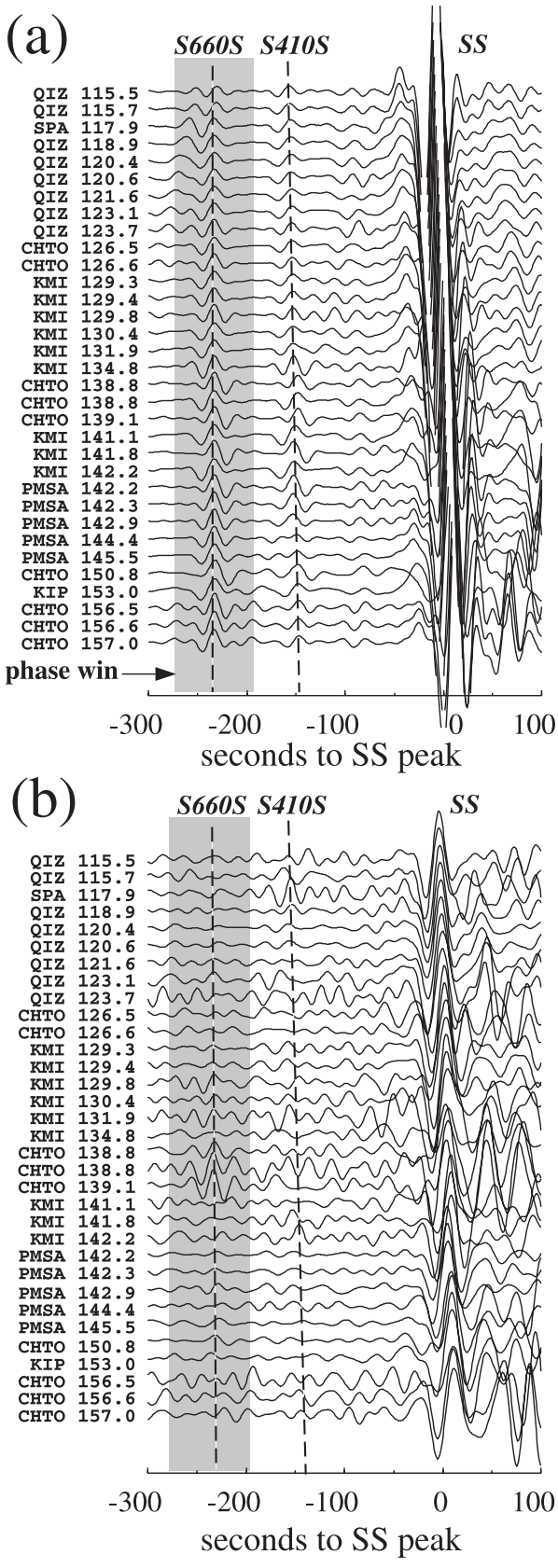

radius) according to their reflection points (see Figure 3a). After deconvolving the instrument responses from the records, we apply a Half-Welch filter to the *SH* component seismograms with cutoff frequencies at 15 and 100 s and peak frequencies between 20 and 35 s (Figure 3b). Figure 3c shows predicted and observed *S*, *S*660*S*, *S*410*S*, and *SS* arrivals on sample *SH* component records after filtering. In this example, the observed differential travel time of *S*410*S* – *S*660*S* is ~11 s shorter than that predicted by PREM; this suggests a narrower TZ near the reflection point than that predicted by PREM (270 km), though the effect of lateral heterogeneities, up to ±2 s, cannot be ignored.

3.1. Measurement Procedures

[15] Our new align-and-stack approach is as follows:

1. Align the observed and synthetic seismograms on the first major swing of the *SS* phase. The seismograms are then edited interactively; the polarity is reversed if necessary. This step helps to remove source and station effects [e.g., *Shearer*, 1993].

2. The goal of this step is to align the *S*660*S* waveforms as well as possible. We first apply an epicentral distance correction (to the data and synthetic seismograms) using predicted *SS*–*S*660*S* times and a reference distance of 130°. We then apply corrections to the data seismograms to account for the effect of surface topography (using ETOPO5 database distributed by National Geophysical Data Center) and crust (using CRUST5.1 of *Mooney et al.* [1998]). Sample arrays of synthetic and data seismograms are shown in Figure 4. The scales of the data seismograms are adjusted slightly for a better visual examination. The synthetic seismograms (Figure 4a) show clear underside reflections from the 660 and 410 (at 670 and 400 km, respectively, for PREM). Peak arrivals of *SS* vary around 0 s as a result of the move out corrections for *SS*–*S*660*S*. Determination of the locations of these secondary arrivals in the data seismograms (Figure 4b) is often more difficult due to the presence of noise. Some seismograms, e.g., three records from CHTO with distances between 138.8° and 139.1°, show particularly high amplitudes for the *S*660*S* phase. The majority of the records, however, show considerable complexities in the waveforms and travel times of these phases, especially for *S*410*S*. Therefore stacking is necessary to ensure the quality of our measurements.

Figure 4. (opposite) Sample arrays of synthetic (computed using PREM) and observed seismograms for the cap location of (−35° N, 149° E). All seismograms have been shifted to aligned on *S*660*S* based on the predicted times of *SS*–*S*660*S*. The station names and source-receiver distances are listed on the left of the records. The shaded region shows a 85 s phase window surrounding the *S*660*S* waveform; this window is used in computing autocorrelation functions (see text for details). The dashed lines mark the predicted peak locations of *S*410*S* and *S*660*S*. (a) PREM synthetic seismograms. (b) Data seismograms which show more complexity in the waveforms and travel times of *S*410*S* and *S*660*S*. Corrections for source–receiver distances have been applied to both the synthetic and data seismograms based on the predicted *S*410*S* – *S*660*S* times. Additional corrections have been applied to the data seismograms to account for crustal thickness and the surface topography.

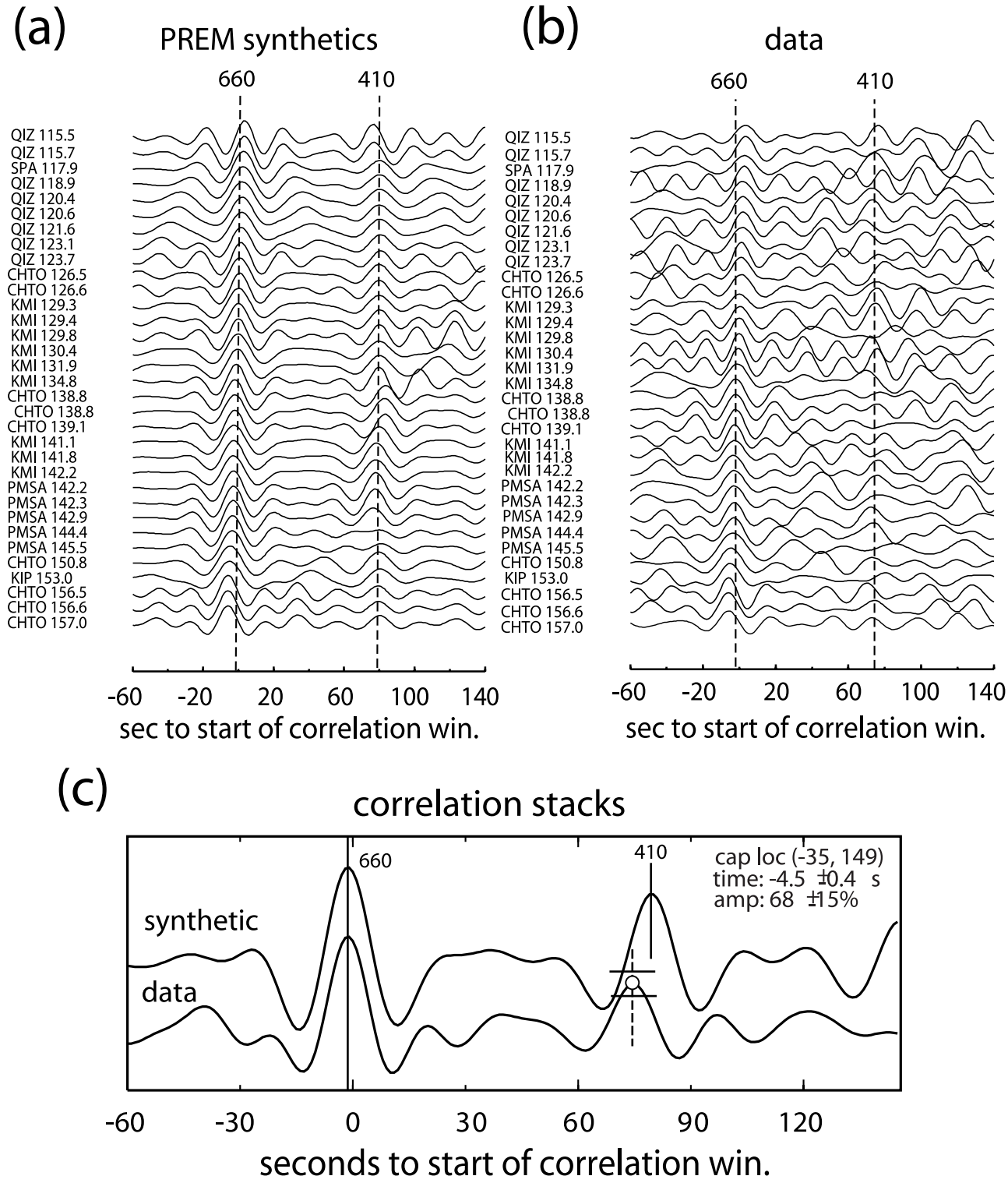

Figure 5. Autocorrelation functions calculated from correlating the *S*660*S* waveforms for (a) the synthetic and (b) the data seismograms. The dashed lines mark the predicted peak locations of *S*410*S* and *S*660*S*. (c) Stacks of autocorrelation functions from Figures 5a and 5b. Travel time residual of *S*410*S*–*S*660*S* can be readily measured from the time shift between the observed (dashed line) and synthetic (solid line) correlation peaks associated with the 410. The error bars represent the uncertainty associated with the amplitude measurement for this cap.

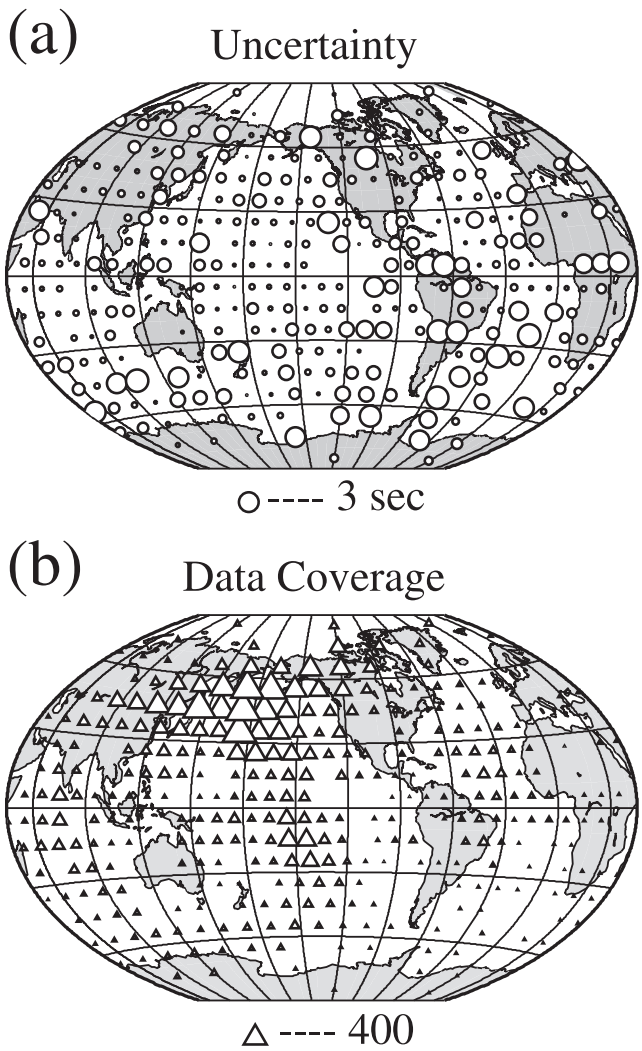

Figure 6. (a) Uncertainties (in seconds) at 311 cap locations. High quality measurements are evident in Eurasia and northern Pacific. The Southern Hemisphere, particularly the southern Atlantic and Indian Oceans, has the largest uncertainties due to sparse data coverage. (b) Data coverage for the same caps shown in Figure 6a. The best coverage is in the northern Pacific region; the sparsest coverage is in the southern Atlantic Ocean.

3. Instead of stacking for *S*660*S* using the original waveforms, we autocorrelate each seismogram with the waveform enclosed in a fixed time window of 85 s, 42.5 s on each side of the predicted *S*660*S* peak at a reference distance of 130° (see shaded region in Figure 4). This operation is carried out on all of the synthetic and data seismograms. The relatively wide autocorrelation window accounts for potential path effects and a possible misalignment of *SS* in step 1. Because of the similarities in the underside reflections from the 410 and 660, one could expect a reasonable correlation, in spite of the inherent noise, between the waveforms of *S*410*S* and *S*660*S*. We use the expected correlation peak at the beginning of the correlation window to normalize each autocorrelation function.

4. We apply an additional move out correction for *S*410*S*−*S*660*S* relative to a reference distance of 130°. The

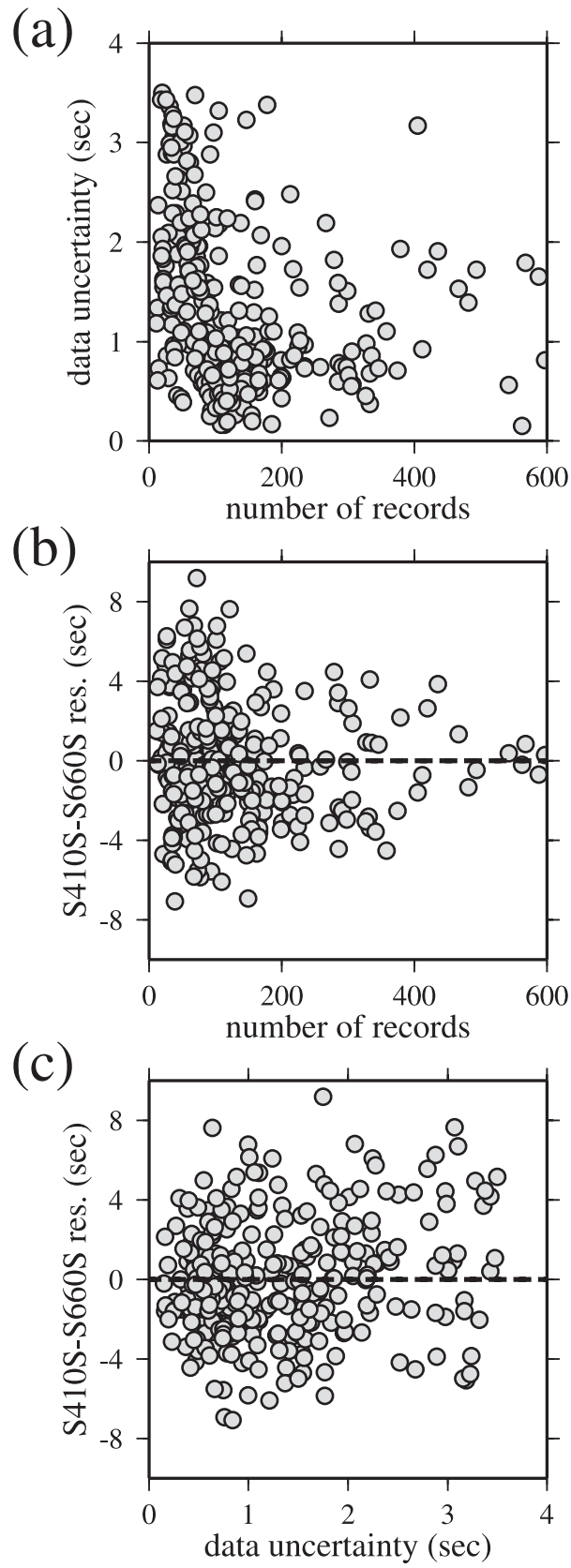

Figure 7. (a) Measurement uncertainties as a function of the number of observations. (b) Travel time residuals of *S*410*S*−*S*660*S* as a function of data density. (c) Travel time residuals of *S*410*S*−*S*660*S* as a function of data uncertainties.

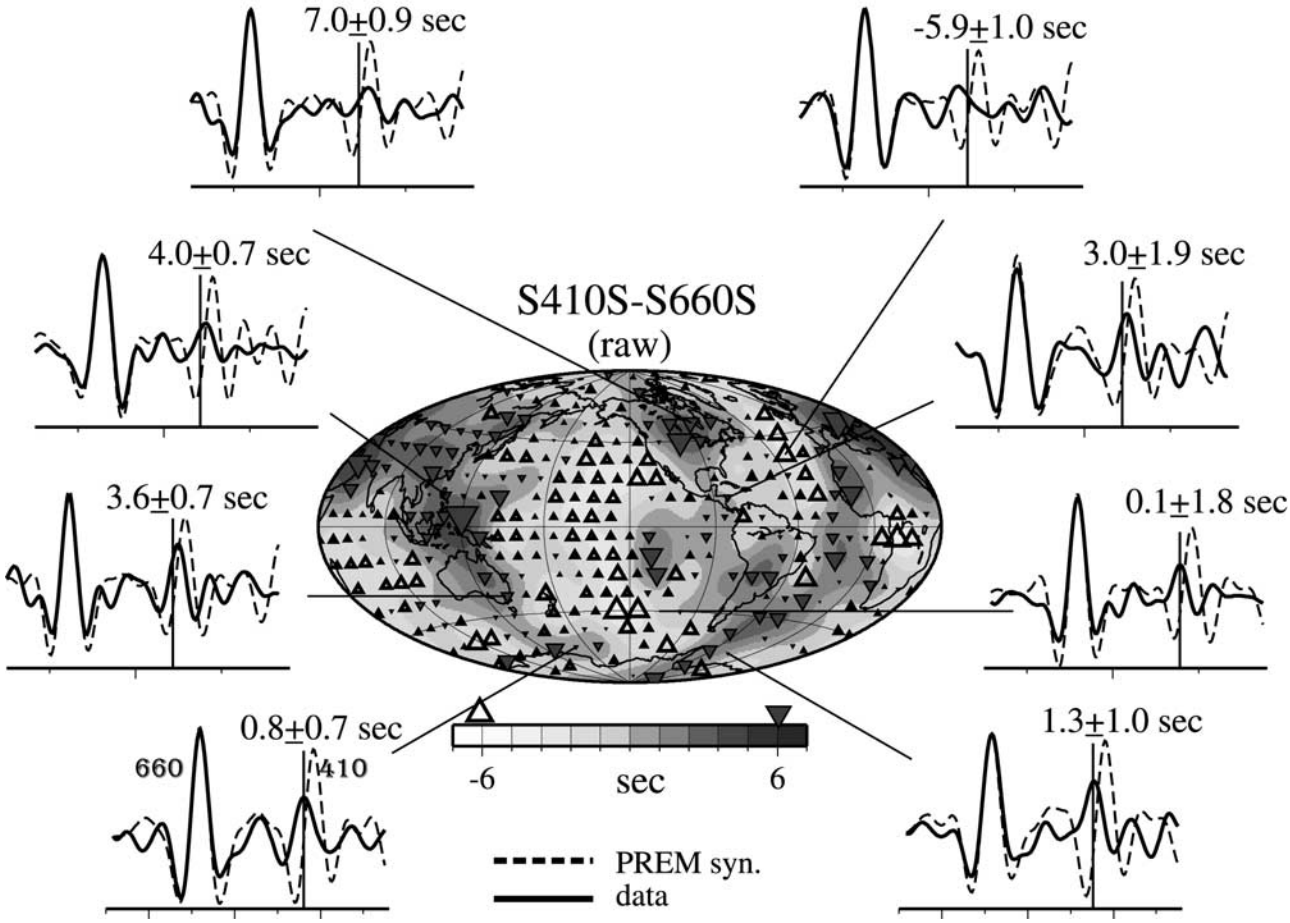

Figure 8. A global map of *S*410*S* – *S*660*S* without correcting for the velocity variations within the TZ. Red (or blue) triangles represent places where the TZ is thinner (or thicker) than the global average. The cap residuals are interpolated using a degree 12 spherical harmonic expansion. Sample stacks of synthetic and data autocorrelation functions are shown in red and black, respectively. The locations of the selected caps are indicated by the straight lines that connect the map locations with autocorrelation stacks. The *S*410*S*–*S*660*S* residuals are measured from the time shifts between the data and synthetic 410 correlation peak. The travel times reported here have removed the global average of −8.1 s (marked by the vertical line on each pair of autocorrelation stacks). See color version of this figure at back of this issue.

resulting traces are then evaluated interactively on the basis of amplitude variations and frequency content. We discard traces that appear to be highly oscillatory since they usually result from high noise levels in the original acceleration seismograms. On occasion anomalously broad 660 correlation peaks can be observed, which indicate that the original *S*660*S* waveforms were not properly enclosed in the 85 s correlation window. This ''misfire'' could result from possible misalignment of *SS* in step 1 or from anomalously large variations of velocity and boundary topography. These defective autocorrelation functions are discarded also. Sample autocorrelation functions resulting from the acceleration seismograms in Figure 4 are shown in Figure 5. The synthetic results (Figure 5a) show two pronounced peaks associated with the 410 and 660. The dotted lines mark the locations of the two major peaks in the final synthetic stack (see Figure 5c). Note that the 660 peaks shift from right to left as epicentral distances increase. This is a direct result of the move out corrections of *S*410*S*–*S*660*S*. The autocorrelation functions generated from data seismograms (see Figure 5b) show much larger variations in the locations of the 410 peak.

5. We stack the synthetic and data autocorrelation functions (see Figure 5c), respectively. Both stacks show pronounced arrivals resulting from the 410 and 660. The travel time residual of *S*410*S*–*S*660*S* can be readily measured from the time shift between the data (dashed line) and predicted (solid line) 410 peaks located nearly 75 s after the start of the correlation window.

[16] The above approach requires a relatively high correlation between *S*410*S* and *S*660*S*. The data selection process is more stringent than those based only on signal-to-noise ratios. One distinct advantage of correlating *S*660*S* with *S*410*S* (rather than with *SS*) is that the autocorrelation functions are not affected by possible errors in the determination of the polarity of *SS* in step 1. Furthermore, stacks obtained using our approach are nearly insensitive to potential complexities, largely due to crustal reverberations, in the *SS* waveforms. It should be remembered that the purpose of the corrections for surface

topography and crustal thickness (see step 2) is to enhance the alignment of the *S*660*S* waveforms for further processing. While these two sets of corrections may improve the stability of our method, the final measurements of *S*410*S*–*S*660*S* which use a fixed correlation window are virtually independent of the individual or averaged correction values.

3.2. Error Analysis

[17] We use a "bootstrapping" technique [*Shearer*, 1993] to estimate the uncertainties in our measurements. For each cap we randomly pick the same number of traces from the pool of quality autocorrelation functions that satisfy all the selection criteria. We then measure the differential travel times of *S*410*S* – *S*660*S* on the bootstrapped stacks and obtain a distribution of values. The mean of these bootstrapped values is used as the final *S*410*S*–*S*660*S* time for this cap, and the standard deviation provides an effective measure of the uncertainty. Figure 6a shows a global map of the uncertainties in the *S*410*S*–*S*660*S* times; only 311 measurements with uncertainties <3.5 s are considered quality measurements. In general, measurements in the Northern Hemisphere are more reliable than those in the Southern Hemisphere. The measurement uncertainties are particularly low in the northern Pacific Ocean, North America, and Eurasia, whereas caps in the southern Atlantic and Indian Oceans have much higher uncertainties. The best coverage (Figure 6b) is in the northern and central Pacific Ocean, while a sparse coverage is evident in parts of South America and the southeast Pacific. In general, measurements in poorly covered regions have relatively high uncertainties.

[18] A modest negative correlation is observed between the measurement uncertainties and the number of seismograms for caps that contain less than 150 records (see Figure 7a). The majority of our measurements, however, have uncertainties of 2 s or less, without notable effects from the data count. Perturbations in *S*410*S*–*S*660*S* times do not appear to correlate with the number of seismograms (Figure 7b). The range of perturbations decreases slightly for caps that contain large number of seismograms. This is partly due to the fact that many of these caps are in the same geographical area (northern Pacific), where the *S*410*S*–*S*660*S* residuals are only marginally smaller than the global average (see section 4 for details). Our measurements of *S*410*S*–*S*660*S* are not biased by the uncertainties, as shown in Figure 7c. The range of *S*410*S*–*S*660*S* variations is nearly constant with respect to data uncertainties, e.g., the range of variations for caps with uncertainties ~1 s is nearly the same as those with ~3 s uncertainties. No major offset is evident away from the zero line.

4. Global *S*410*S* – *S*660*S* Residuals

[19] A global map of raw *S*410*S*–*S*660*S* travel time residuals, without correction for velocity perturbations in the TZ, is shown in Figure 8. An average offset of −8.1 s, relative to that predicted by PREM, is removed from the residuals. The color contours in the background show a degree-12 spherical harmonic expansion of the cap residuals. Significant positive perturbations relative to the global average are observed under the western Pacific, Eurasia, South Atlantic, and North America. Anomalies with perturbations >8 s and lateral dimensions >3000 km are present under the western Pacific and African Rift Zone. The locations and dimensions of these anomalies appear to follow the reported fast velocities in the transition zone [e.g., *Su et al.*, 1994; *Gu et al.*, 2001a]. Negative perturbation of significant lateral scales are observed under the Pacific and northern Atlantic Oceans. Sample correlation stacks in Figure 8 show variations from −6 to 7 s from the global average. The correlation peaks that result from the 410 vary greatly both in shape and in arrival time; this suggests considerable complexities on the TZ discontinuities.

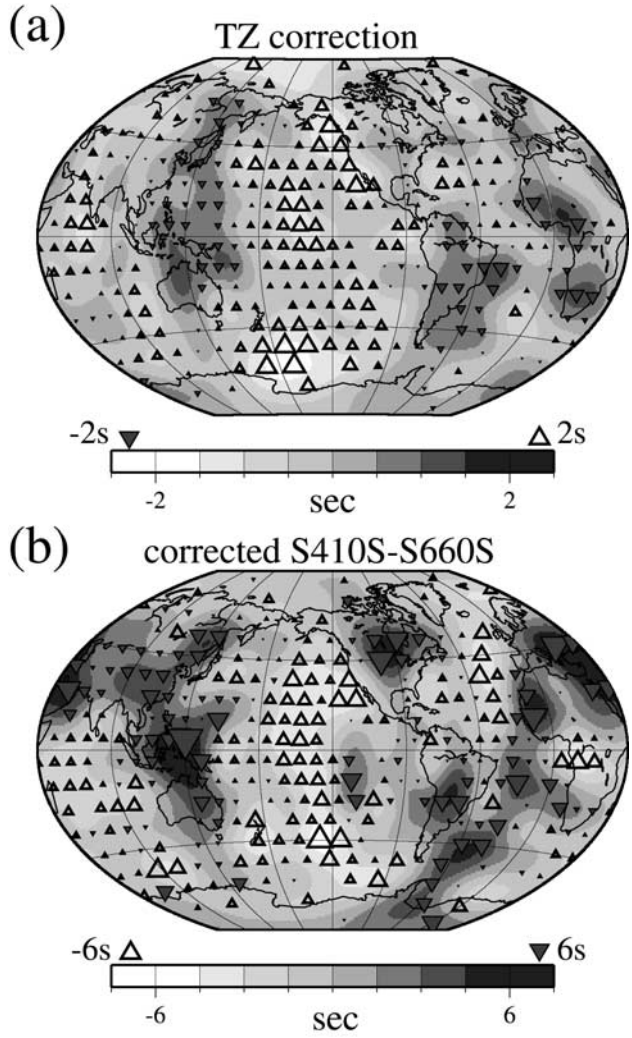

Figure 9. (a) Travel time corrections for the TZ structure, as predicted by S12/WM13 of *Su et al.* [1994]. The velocity perturbations at 550 km is plotted on the background. The triangles represent the correction values at the cap centers. Most corrections have absolute values of 2 s or less. (b) Residual of *S*410*S*–*S*660*S* after correcting for TZ velocity structure. The color conventions are the same as those of Figure 8. The range of *S*410*S*–*S*660*S* perturbations becomes slightly larger after the correction. See color version of this figure at back of this issue.

[20] There is evidence for the intermittent presence of the 520 in the oceanic stacks [e.g., *Shearer*, 1996; GDA98]. For

example, stacks under the Arctic and western and southern Pacific Oceans (see Figure 8) show small correlation peaks between those associated with the 410 and 660. The amplitudes of these reflections are generally small, which indicate that the 520 is either a weak reflector or a reflector with strong depth variations. The 520 reflection is, however, notably absent in most of the continental stacks, for example, in North and Central America. The preferential detection of the 520 was reported by GDA98 as evidence for potential thermal/chemical differences between continent and oceans at depths below 400 km. A recent study by *Deuss and Woodhouse* [2001] suggested the presence of two mild reflectors between the 410 and 660, most notably under the continents. While our study does not focus on the 520, its low-reflection amplitude in our continental stacks appears to suggest, at least, significant complexities in the radial seismic signatures within the TZ.

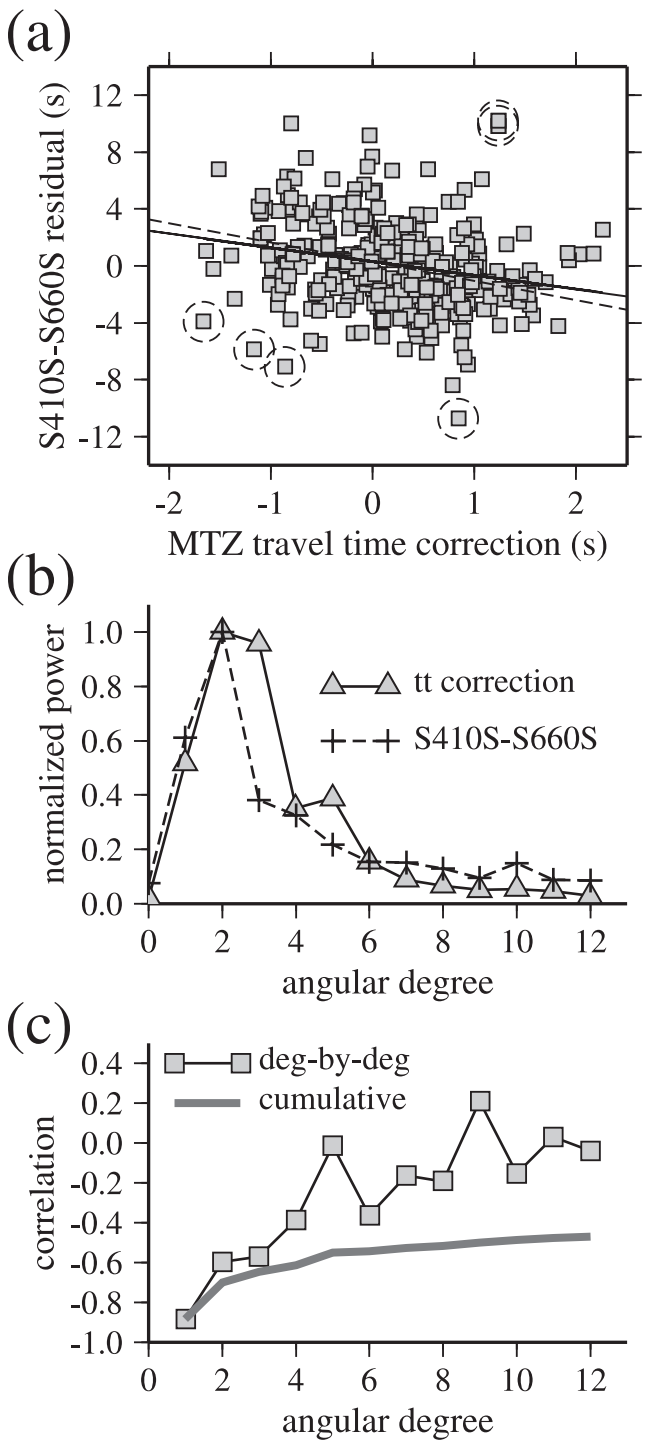

Figure 10. (opposite) (a) Raw measurements of *S*410*S*–*S*660*S* (without correcting for transition zone velocity structure) as a function of TZ travel time corrections. The solid line represents a least squares fit of all values with a slope of −0.96±0.23; the correlation coefficient is −0.23. The dotted line represents a least squares fit after removing six outliers (circled). The slope is −1.35±0.21 and correlation is −0.35. (b) Normalized power spectra of the raw *S*410*S* – *S*660*S* residuals and TZ travel time corrections. Both spectra show strong signatures at the degree-1 and degree-2 spherical harmonics. (c) Degree-by-degree and cumulative correlations between the spherical harmonic coefficients and the raw *S*410*S*–*S*660*S* residuals and those of the TZ travel time corrections. A negative cumulative correlation implies considerable influence from the TZ thermal structure on the topography of the 410 and 660 (see text for details).

4.1. TZ Travel Time Correction

[21] To account for the effect of velocity structure, we compute two-way *S* travel time using S12/WM13 (will be referred to as S12 and *Su et al.* [1994]) for a shear wave that travels through the TZ under each cap location. We assume a reference distance of 130°. This velocity model is reasonably well constrained by both the travel time, primarily *S* and *SS*, and the waveform data that are sensitive to the TZ structure. The TZ structure predicted by S12 is generally consistent with other existing shear velocity models [e.g., *Li and Romanowicz*, 1996; *Liu*, 1997; *Ritsema et al.*, 1999], both in the location and the amplitude of large-scale anomalies. The corrections are typically <2 s (Figure 9a). The corrected *S*410*S* – *S*660*S* residuals (see Figure 9b) show slightly larger variations than the raw residuals, though most of the long-wavelength features are consistent. The global average of the corrected residuals is −8.3 s relative to PREM.

[22] There is a modest negative correlation between the raw *S*410*S* – *S*660*S* residuals and the travel time corrections, −0.24 if all residuals are considered (Figure 10a). The solid line represents a least squares fit of the residuals with a slope of −0.96 ± 0.23. If we exclude six outliers (residuals that are enclosed in dotted circles), the correlation becomes −0.35, which is statistically significant with a confidence level >95%. The best fit line (dotted) shows a slope of −1.4 with a standard deviation of 0.2.

[23] The normalized power-spectral amplitudes of the raw *S*410*S*–*S*660*S* residuals correlate well with those of the TZ corrections in degrees 1 and 2 (Figure 10b). There is a negative overall correlation (∼−0.5) between the coefficients of their spherical harmonic expansions, particularly at the low-degree harmonics that contain the highest energy (Figure 10c). This negative correlation becomes more pronounced after we apply the TZ corrections to the raw *S*410*S*–*S*660*S* residuals (not shown). It suggests consider-

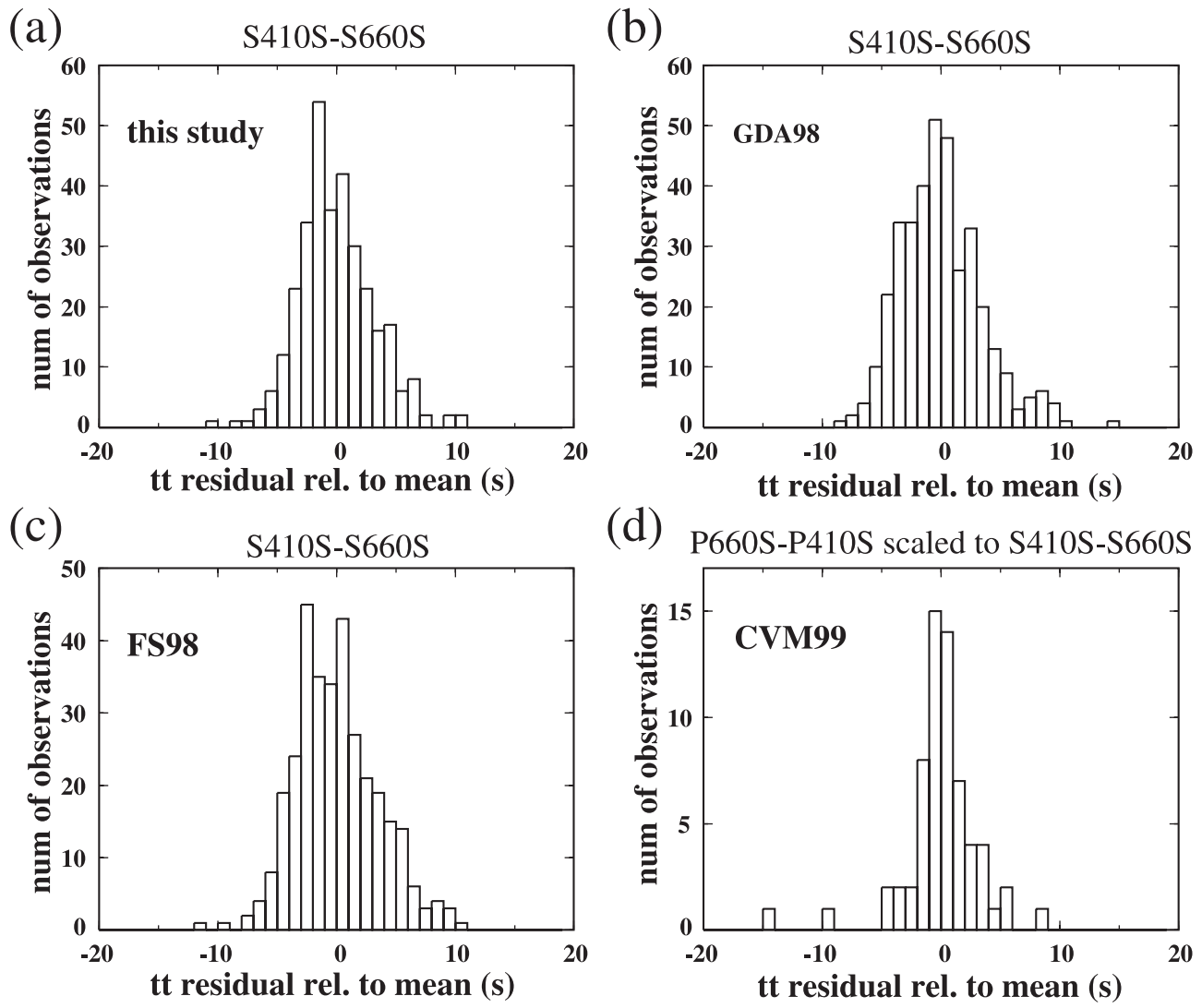

Figure 11. Distributions of the *S*410*S* – *S*660*S* measurements of (a) this study, (b) GDA98, and (c) FS98. All three distributions are nearly normal with significant variations from the mean. (d) Distribution of modified *P*660*s*–*P*410*S* residuals from CVM99. We have multiplied the original residuals of CVM99 by a factor of 3.2. This is to account for the smaller sensitivity of converted waves (in comparison with *SS* precursors) to a boundary undulation. There are few measurements in CVM99 with amplitudes beyond ±2 s from the mean; this is inconsistent with the distributions shown in Figures 11a–11c.

able influences of TZ thermal structure on the topography of the 410 and 660.

4.2. Distribution of *S*410*S*–*S*660*S*

[24] Perturbations of the corrected *S*410*S*–*S*660*S* times show a semi-normal distribution with peak-to-peak residual values exceeding 20 s (Figure 11a). The large standard deviation of this distribution implies the undulating nature of TZ thickness on a global scale. Such level of variations is consistent with those of GDA98 (Figure 11b) and FS98 (Figure 11c), even though they were obtained using a different approach. All three distributions, however, show significantly larger variations than those of CVM99 using *Pds* waves (Figure 11d). Only few observations in the latter study extend beyond ±2 s from the their global average. The original residuals of CVM99 have been scaled to *S*410*S*–*S*660*S* by a factor of 3.2 to account for the different sensitivities to boundary undulations between *SS* precursors and *Pds* waves.

5. Global Variations of TZ Thickness

[25] To convert the corrected *S*410*S*–*S*660*S* times into TZ thickness variations, we express the depth perturbation of a boundary as a function of the travel time residual δt,

$$\delta h_i = \frac{\delta t_i r_i}{2(\eta_i^2 - p_i^2)^{\frac{1}{2}}}, \tag{1}$$

where i represents a given discontinuity, $\eta_i = r_i/v(r_i)$ and p_i is the ray parameter [*Dziewonski and Gilbert*, 1976]. We use a ray parameter of 12.0 and 11.8 s/deg for the 410 and 660,

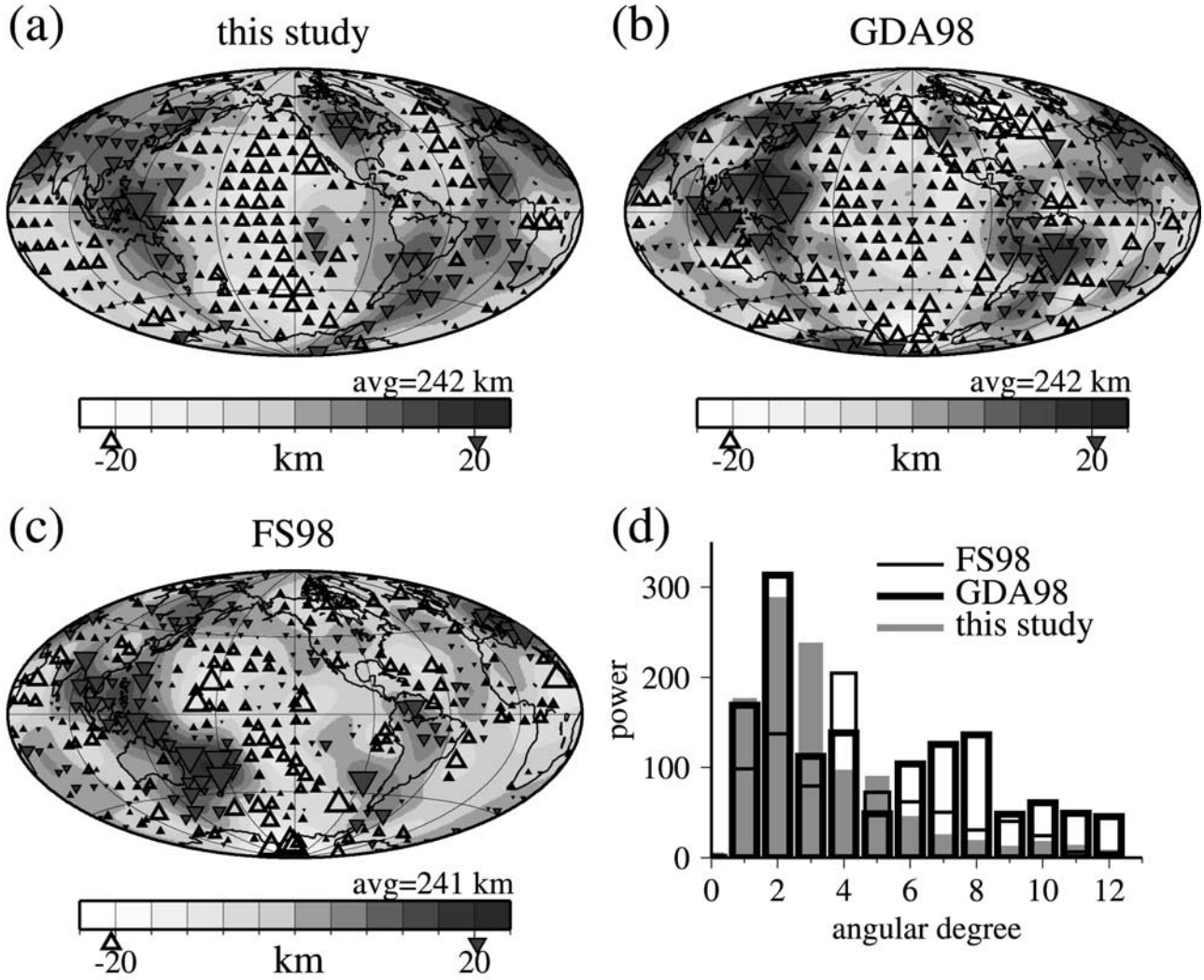

Figure 12. Thickness maps of the TZ. In each map, the residuals have been interpolated using a spherical harmonic expansion up to degree 12. The blue and red contours show the regions of thick and narrow TZ, respectively. (a) Thickness variations inferred from *S*410*S*–*S*660*S* residuals of this study. (b) Thickness variations in GDA98 inferred from *SS*–*SdS* residuals. (c) Thickness variations in FS98 inferred from *SS*–*SdS* residuals. Only caps with more than 20 records are shown. (d) Power spectra of all three thickness maps. The long-wavelength features are fairly consistent among these maps, as suggested by the agreement at the low-degree spherical harmonics. See color version of this figure at back of this issue.

respectively, assuming a reflected shear wave with a reference distance of 130°.

[26] We obtain an average thickness of 242 km for the TZ. This value agrees perfectly with those of GDA (242 km) and FS98 (241 km), but is significantly narrower than that of CVM99 (250 km). In Figure 12 we compare the measurements of TZ thickness from three recent global studies of *SS* precursors. To first order, the global pattern of the long-wavelength variations obtained from this study (Figure 12a) are consistent with those of earlier results (Figures 12b and 12c). All three maps show significantly increased thickness in the northwestern Pacific, Indonesia, and western Europe. A narrow TZ is generally observed in the central Pacific and Africa. It is encouraging that the main features of this study are more laterally coherent than those in the earlier studies; this suggests more effective cap averaging, owing mostly to the improved data coverage on a global scale. Regional differences do exist, however, particularly in the amplitude of the variations. For example, our new measurements show less pronounced variations in the western Pacific than GDA98. This discrepancy likely results from complexities in the TZ shear velocity and boundary topography near major subduction zones. Another major difference among these studies is in New Zealand and Tonga-Kermadec islands, where FS98 shows a markedly thicker TZ than the other two studies. The source of this discrepancy is unknown, though higher uncertainties of the measurements due to the restrictive data coverage in this region (see Figures 6a and 6b) could be a factor.

[27] The power spectra of these three maps (Figure 12d) show pronounced signatures at the low-degree harmonics. Similar to the raw *S*410*S*–*S*660*S* residuals, the thickness measurements of this study are dominated by degrees 1–3,

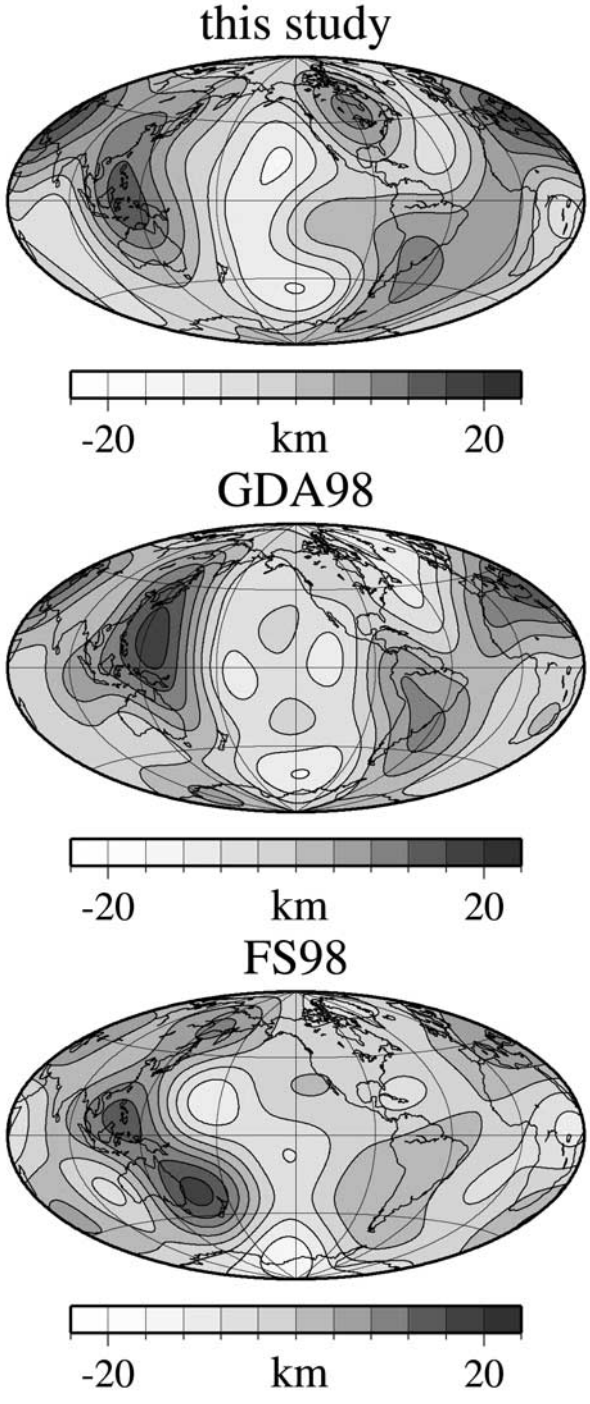

Figure 13. A low-pass filtration of the thickness maps (see Figure 12) up to the degree-6 spherical harmonic. The amplitude and shape of the long-wavelength features are consistent among these maps, particular among this study and GDA98.

and the spectral amplitudes at degrees 1 and 2 correlate well with those of GDA98. In comparison, the overall amplitudes of FS98 are slightly smaller and strong signals are observed at degrees 2 and 4. A low-pass filtration of the thickness maps (truncated at the degree-6 spherical harmonic) is shown in Figure 13. All three maps show strongly positive perturbations in the western Pacific, South America, and western Eurasia. The most consistent large-scale negative perturbations are evident under the Pacific and northern Atlantic Oceans, demonstrating a strong correlation among these measurements at the longest wavelengths.

[28] For a detailed comparison with the global maps of GK96 we compute the average TZ thickness from adjacent caps. This procedure provides an effective averaging area of $\sim$900 deg^2, similar to that used in the former study (see Figure 14). This low-pass filtration leads to a reduction of TZ thickness variations (see Figure 14a). Excellent agreement, particularly in the Pacific, Indian Ocean, and North America, is observed between these two studies, despite differences in the cap locations. More importantly, this

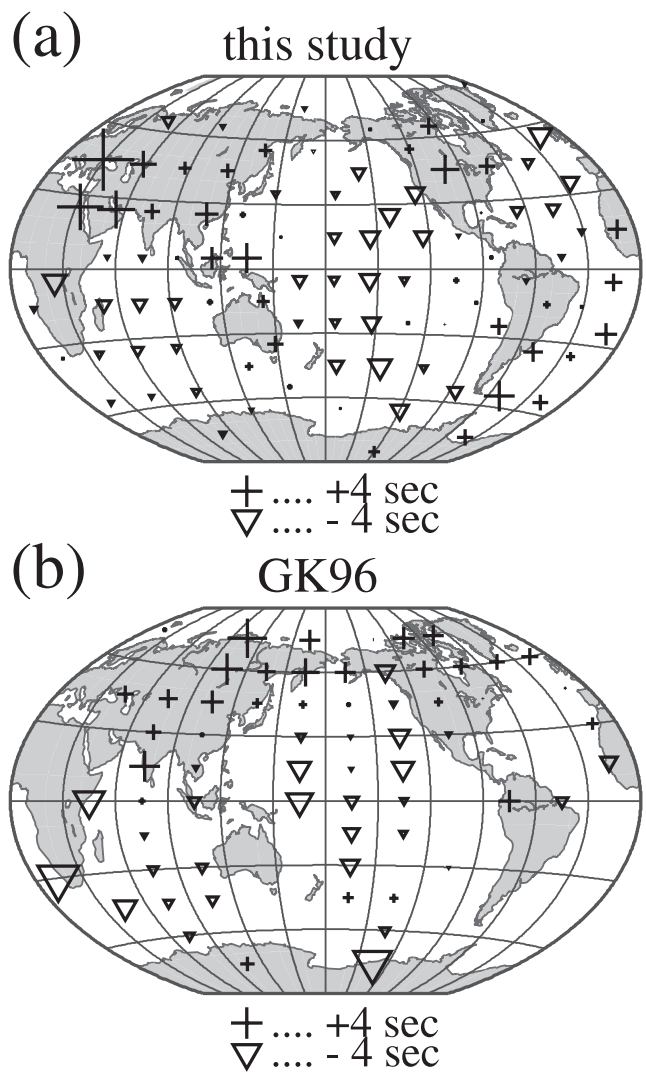

Figure 14. (a) A low pass filtration of our *S*410*S* – *S*660*S* residuals obtained by averaging neighboring caps (up to 5). The new ''footprints'' are nonoverlapping and have effective averaging areas of $\sim$900 deg^2 (as opposed to 314 deg^2 in the original scheme). (b) Global measurements of *S*410*S* – *S*660*S* from GK96. The range of variations is consistent between these two studies. Note that neither data sets shown here have been corrected for TZ velocity perturbations.

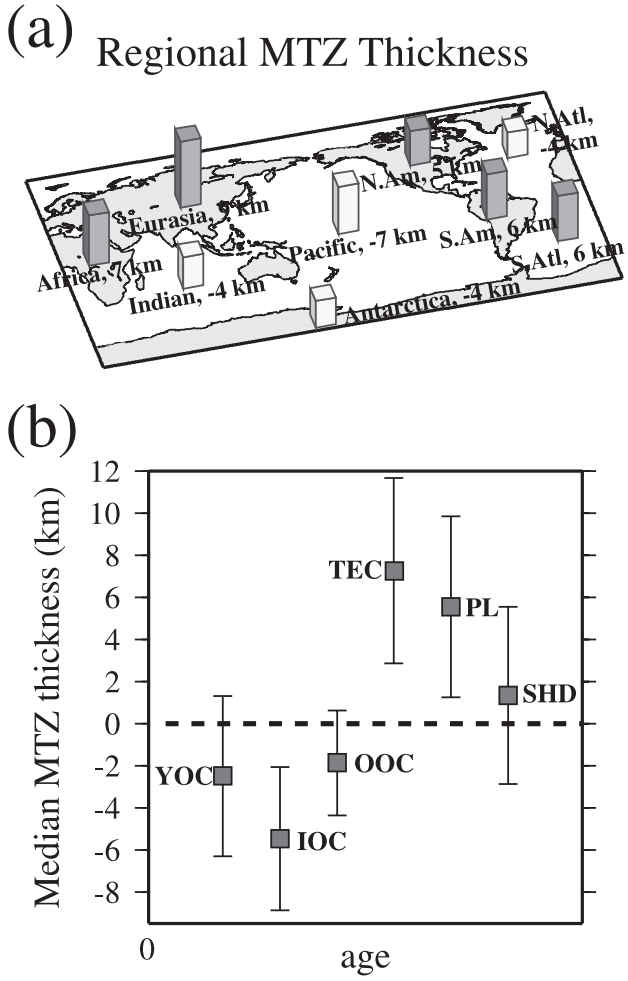

Figure 15. (a) Regionally averaged thickness of the TZ. Positive and negative values represent regions of thicker and thinner TZ, respectively. TZ under the continental regions, e.g., Eurasia and Africa, is significantly thicker than that under vast oceanic regions. (b) The median of the TZ thickness measurements for six tectonic regions proposed by the regionalization scheme of *Jordan* [1981]. The abbreviated names are defined as follows: YOC, young ocean; IOC, intermediate aged ocean; OOC, old ocean; TEC, tectonic regions; PL, platforms; and SHD, shields. A significant continent–ocean difference is evident, although the thickness of the TZ does not appear to correlate with the age of the crust.

simple experiment provides an explanation for the amplitude discrepancy of the global variations between GK96 (smaller) and other studies of *SS* precursors (larger). It does not, however, explain the amplitude difference between this study and CVM99 since the latter study used much smaller averaging areas.

6. Regional Thickness Variations

[29] One of the most intriguing puzzles in mantle dynamics is the depth to which continental lithosphere is distinct in the upper mantle. Results obtained from global seismic tomography show that the continent–ocean difference persists down to 250 km, and perhaps deeper [e.g., *Woodhouse and Dziewonski*, 1984, 1989; *Su et al.*, 1994; *Li and Romanowicz*, 1996]. Studies using secondary reflected and converted phases have provided important constraints on the depth extent of surface tectonics. For example, GK96 suggested that the transition zone is nearly 14 km thicker under Asia and North America than under the neighboring Pacific. GDA98 detected a regional 520 under the oceans, from which the amplitude of reflections is significantly more pronounced under the oceans than it is under the North American and African shields. The preferential detection of the Lehmann discontinuity (also referred to as the 220) beneath continents, reported by recent studies of *SS* precursors [*Deuss and Woodhouse*, 2000; *Gu et al.*, 2001b], provides further evidence for possible differences in rheology or composition between oceans and continents at depths below 200 km.

[30] Regional averages of TZ thickness (Figure 15a) show peak-to-peak variation of 16 km between continental (e.g., 9 km in Eurasia and 7 km in Africa) and vast oceanic regions (e.g., −7 km in the Pacific and −4 km in the Indian Oceans). The Atlantic Ocean shows an anomalous increase of TZ thickness from the north to the south. The location of the thickened TZ in the southern Atlantic coincide with that of fast TZ velocities; both of which could be associated with the potential presence of cold, recycled oceanic lithosphere in the TZ.

[31] *Gurrola and Minster* [1998] reported a thickness variation (of the TZ) exceeding 30 km between Obninsk, Russia, and Pasadena, California. While we do not have a reliable measurement under California, our regional estimate in the western Eurasia, 10–15 km thicker than the global average, is comparable with the result from their study (252 km). The thickened TZ in this region may be associated with the high-velocity anomalies above and within the TZ.

[32] We further divide our measurements according to the regionalization scheme of *Jordan* [1981]. The median of the perturbations in each tectonic region is shown in Figure 15b. We observe a notable continent–ocean difference: the transition zone is, on average, 6–8 km thicker under continents than under oceans. If we assume an olivine composition with 90% Mg_2SiO_4 and 10% Fe_2SiO_4, this thickness variation would translate to a difference in temperature of 50–70°C between oceans and continents. The TZ width does not correlate, however, with the age of the crust. For example, TZ under tectonic regions is ~6 km thicker than that under shields.

7. Discussion and Conclusions

[33] It is not the aim of this study to image the individual topography of TZ discontinuities as earlier studies have done using *SS* precursors. Our modeling approach is designed to provide a less velocity-dependent measure of TZ thickness, using a significantly improved *SS* precursor data set. In view of a recent debate [GDA98; FS98; CVM99], we have focused on the robust long-wavelength features and the global variability of TZ thickness. The resolution of our approach is constrained by the wavelengths of *SS* precursors (1500–2000 km laterally); this is

slightly larger than the lateral resolution of recent tomographic studies [e.g., *Ritsema et al.*, 1999; *Masters et al.*, 2000; *Gu et al.*, 2001a].

[34] Thickness variations inferred from our global measurements of *S*410*S*–*S*660*S* are inconsistent with a "flat" TZ; peak-to-peak variations over 25 km are observed. The large-scale features of our measurements are generally consistent with those of GDA98 and FS98, and a low-pass filtration of our cap averages shows a global pattern and variability comparable with the results of GK96. However, the thickness variations observed in this study are much greater than those of CVM99 (<10 km). It is not clear if this discrepancy results from differences in data coverage, measurement uncertainty, or data resolution/sensitivity to boundary perturbations. It is conceivable that some of the observations in CMV99 are significantly affected by their choice of the *P* and *S* velocity models. Differences in the size of the Fresnel zones between *SS* precursors and *Pds* waves may also be a factor, as the finer-scale variations observed by CVM99 are mostly averaged out in our study. Furthermore, it is possible that due to the small-scale nature of the short-period *Pds* waves and a relatively sparse global coverage, some of the strongest local variations are left unimaged by CVM99 in a laterally complex TZ. Recent studies on the plumes under Hawaii [*Li et al.*, 2000a] and subduction zone under Japan [*Li et al.*, 2000b] show *Pds* travel time variations from less than 19 s to greater than 26.5 s. This translates to thickness ranging from 210 km to 280 km in scale lengths of a few hundred kilometers. Such roughness on a local scale could be present also under the continental regions, e.g., Europe, where *van der Lee et al.* [1994] reported a lack of *P*660*s* in the array data. Furthermore, D. Suetsugu et al. (Probing the "Superplume" beneath the South Pacific, submitted to *IRIS Newsletter*, 2001) combined reflected and converted phases and provided further evidence for large perturbations (~30 km) in TZ thickness under the South Pacific Superswell region. This range of variations is equivalent to a temperature perturbation of 200–300 K, which could be associated with the presence of hot mantle plumes in the transition zone. A similar range of variations is recently reported by H. J. Gilbert et al. (The presence of layered convection as inferred from the upper mantle thermal structure below the western United States, submitted to *Journal of Geophysical Research*, 2002) in the western United States.

[35] The power of the global TZ thickness is dominated by low-degree (1–4) spherical harmonics. This spectral characteristic is consistent with that of TZ velocities predicted by recent tomographic models [e.g., *Masters et al.*, 2000; *Mégnin and Romanowicz*, 2000; *Gu et al.*, 2001a], especially the degree 2 spherical harmonic. Our analysis shows a slight anticorrelation between the *S*410*S*–*S*660*S* residuals (or TZ thickness) and the two-way shear wave travel times or most likely, thermal variations, within the TZ. This implies considerable effects of temperature on the depths of the TZ discontinuities. The fact that this is only a mild anticorrelation implies that a significant fraction of TZ thermal anomalies may be limited in the radial extent; that is, anomalies of different origins (and temperatures) may be influencing the phase transitions near the 410 and 660. The 660 is strongly influenced by thermal variations in the lower half of TZ; this is clearly observed near major subduction zones where accumulation of cold subducted material may be occurring [e.g., *Shearer and Masters*, 1992]. On the other hand, the topography of the 410 is mostly sensitive to velocity variations in the depth range of 350–450 km. There is a greater complexity and a lower amplitude in the topography of this boundary, which could be partly attributed to trade-offs between thermal and kinematic effects that are associated with the positive Clapeyron slope of olivine α to β-phase transition [e.g., *Yuen et al.*, 1994; *Thoraval and Machetel*, 2000]. TZ thickness could also be influenced by possible compositional heterogeneities close to or within the TZ.

[36] It is still being debated whether the low-degree signatures in TZ thickness (obtained from long-period waves) can be extrapolated to small scales [*Shearer*, 2000], as there is evidence for significant thickness variations at scale lengths of hundreds of kilometers (e.g., near regions of subduction and plumes). *Neele et al.* [1997] and *Chaljub and Tarantola* [1997] raised the concern that small-scale topography on the discontinuities may bias the inferences of large-scale observations from studies of *SS* precursors. By performing synthetic experiments using a longer-period *SdS* data set, *Shearer et al.* [1999] showed that the observed long-wavelength features from *SS* precursors are robust and the residuals are nearly insensitive to extreme velocity anomalies (with a scale length of 300–500 km) in the TZ. More work may be needed to establish the connection between large and small scale variations of TZ thickness, as well as their relation to TZ velocity perturbations of varying scales.

[37] One parameter that should be determined to a higher degree of accuracy is the average thickness of the TZ. Our globally averaged TZ thickness is 242 km; this agrees well with estimates from earlier studies of *SS* precursors but is ~8 km thinner than that of CVM99 (250 km). The discrepancy can be partly explained by differences in the location since the majority of the measurements from CVM99 are continental, where we find the TZ to be 6–8 km thicker than it is under the oceans. Other possible explanations may include differences in wave types, processing methods, resolution, as well as the choice of *P* and *S* velocity models.

[38] Finally, we observe a continent-ocean difference, a clear correlation between TZ thickness and the age of the crust is not seen. This might suggest that only the largest wavelength thermal signatures from surface tectonics can survive the short-term (200 m.y.) recycling and, potentially, affect the observations regarding the TZ. Future improvements can be made to the analysis of this study by simultaneously inverting for mantle velocity structure and the topography of TZ discontinuities. This proposed approach can effectively account for tradeoffs between velocity and boundary topography (Y. J. Gu et al., Simultaneous inversion for mantle shear velocity and topography of transition zone discontinuities, submitted to *Geophysical Journal International*, 2002) and thereby improve our understandings of both issues.

[39] **Acknowledgments.** We thank Göran Ekström, Karen Felzer, Peter Shearer, Rainer Kind, Megan Flanagan, and two anonymous reviewers for helpful comments and suggestions. We also thank Jürgen Gossler and Sebastian Chevrot for providing their data sets. Some of the figures were generated using the GMT mapping software [*Wessel and*

Smith, 1991]. This research is supported by grant EAR98-05172 from National Science Foundation.

References

Benz, H. M., and J. E. Vidale, Sharpness of upper-mantle discontinuities determined from high-frequency reflections, *Nature*, *365*, 147–150, 1993.

Bostock, M. G., *Ps* conversions from the upper mantle transition zone beneath the Canadian landmass, *J. Geophys. Res.*, *101*, 8393–8402, 1996.

Castle, J. C., and K. C. Creager, Topography of the 660-km seismic discontinuity beneath Izu-Bonin: Implications for tectonic history and slab deformation, *J. Geophys. Res.*, *103*, 12,511–12,527, 1998.

Chaljub, E., and A. Tarantola, Sensitivity of *SS* precursors to topography on the upper-mantle 660-km discontinuity, *Geophys. Res. Lett.*, *24*, 2613–2616, 1997.

Chevrot, S., L. Vinnik, and J.-P. Montagner, Global-scale analysis of the mantle *Pds* phases, *J. Geophys. Res.*, *104*, 20,203–20,219, 1999.

Deuss, A., and J. H. Woodhouse, Mantle discontinuities from *SS* precursors, *Eos Trans. AGU*, *81*(48), Fall Meet. Suppl., Abstract S51D-10, 2000.

Deuss, A., and J. Woodhouse, Seismic observations of splitting of the mid-transition zone discontinuity in Earth's mantle, *Nature*, *294*, 354–357, 2001.

Dueker, K. G., and A. F. Sheehan, Mantle discontinuity structure from midpoint stacks of converted *P* to *S* waves across the Yellowstone hot spot track, *J. Geophys. Res.*, *102*, 8313–8327, 1997.

Dziewonski, A. M., and D. L. Anderson, Preliminary reference Earth model, *Phys. Earth Planet. Inter.*, *25*, 297–356, 1981.

Dziewonski, A. M., and F. Gilbert, The effect of small, aspherical perturbations on travel times and a re-examination of the corrections for ellipticity, *Geophys. J. R. Astron. Soc.*, *44*, 7–17, 1976.

Estabrook, C. H., G. Bock, and R. Kind, Investigation of mantle discontinuities from a single deep earthquake, *Geophys. Res. Lett.*, *21*, 1495–1498, 1994.

Flanagan, M. P., and P. M. Shearer, Global mapping of topography on transition zone velocity discontinuities by stacking *SS* precursors, *J. Geophys. Res.*, *103*, 2673–2692, 1998a.

Flanagan, M. P., and P. M. Shearer, Topography on the 410-km seismic velocity discontinuity near subduction zones from stacking of *sS*, *sP*, and *pP* precursors, *J. Geophys. Res.*, *103*, 21,165–21,183, 1998b.

Gossler, J., and R. Kind, Seismic evidence for very deep roots of continents, *Earth Planet. Sci. Lett.*, *138*, 1–13, 1996.

Gu, Y. J., Upper mantle transition zone: structure and topography of discontinuities, thesis, 217 pp., Harvard Univ., Cambridge, Mass., 2001.

Gu, Y., A. M. Dziewonski, and C. B. Agee, Global de-correlation of the topography of transition zone discontinuities, *Earth Planet. Sci. Lett.*, *157*, 57–67, 1998.

Gu, Y. J., A. M. Dziewonski, W.-J. Su, and G. Ekström, Models of the mantle shear velocity and discontinuities in the pattern of lateral heterogeneities, *J. Geophys. Res.*, *106*, 11,169–11,199, 2001a.

Gu, Y. J., A. M. Dziewonski, and G. Ekström, Preferential detection of the Lehmann discontinuity under continents, *Geophys. Res. Lett.*, *28*, 4655–4658, 2001b.

Gurrola, H., and J. B. Minster, Thickness estimates of the upper-mantle transition zone from bootstrapped velocity spectrum stacks of receiver functions, *Geophys. J. Int.*, *133*, 31–43, 1998.

Ito, E., and E. Takahashi, Postspinel transformations in the system Mg_2SiO_4-Fe_2SiO_4 and some geophysical implications, *J. Geophys. Res.*, *94*, 10,637–10,646, 1989.

Jackson, I., Some geophysical constraints on the chemical composition of the Earth's lower mantle, *Earth Planet. Sci. Lett.*, *62*, 143–164, 1983.

Jordan, T. H., Global tectonic regionalization for seismological data analysis, *Bull. Seismol. Soc. Am.*, *71*, 1131–1141, 1981.

Katsura, T., and E. Ito, The system Mg_2SiO_4-Fe_2SiO_4 at high pressures and temperatures; precise determination of stabilities of olivine, modified spinel, and spinel, *J. Geophys. Res.*, *94*, 15,663–15,670, 1989.

Katzman, R., L. Zhao, and T. H. Jordan, High-resolution, two-dimensional vertical tomography of the central Pacific mantle using *ScS* reverberations and frequency-dependent travel times, *J. Geophys. Res.*, *103*, 17,933–17,971, 1998.

Le Stunff, Y., C. W. Wicks, and B. Romanowicz, *P'P'* precursors under Africa: Evidence for mid-mantle reflectors, *Science*, *270*, 74–77, 1995.

Lee, D.-K., and S. Grand, Depth of upper mantle discontinuities beneath the East Pacific Rise, *Geophys. Res. Lett.*, *23*, 3369–3372, 1996.

Li, A., K. M. Fischer, M. E. Wysession, and T. J. Clarke, Mantle discontinuities and temperature under the North American continental keel, *Nature*, *395*, 160–163, 1998.

Li, X.-D., and B. Romanowicz, Global mantle shear velocity model developed using nonlinear asymptotic coupling theory, *J. Geophys. Res.*, *101*, 22,245–22,272, 1996.

Li, X., R. Kind, K. Priestley, S. V. Sobolev, F. Tilmann, X. Yuan, and M. Weber, Mapping the Hawaiian plume with converted seismic waves, *Nature*, *405*, 938–941, 2000a.

Li, X., S. V. Sobolev, R. Kind, X. Yuan, and C. H. Estabrook, A detailed receiver function image of the upper mantle discontinuities in the Japan subduction zone, *Earth Planet. Sci. Lett.*, *183*, 527–541, 2000b.

Liu, X.-F., The three-dimensional shear-wave velocity structure of the Earth's lower mantle, thesis, 202 pp., Harvard Univ., Cambridge, Mass., 1997.

Masters, G., T. H. Jordan, P. G. Silver, and F. Gilbert, Aspherical Earth structure from fundamental spheroidal-mode data, *Nature*, *298*, 609–613, 1982.

Masters, G., G. Laske, H. Bolton, and A. M. Dziewonski, The relative behavior of shear velocity, bulk sound speed, and compressional velocity in the mantle: Implications for chemical and thermal structure, in *Earth's Deep Interior: Mineral Physics and Tomography: From the Atomic to the Global Scale, Geophys. Monogr. Ser.*, vol. 117, edited by S. Karato et al., pp. 63–87, AGU, Washington, D.C., 2000.

Mégnin, C., and B. Romanowicz, The 3D shear velocity structure of the mantle from the inversion of body, surface, and higher mode waveforms, *Geophys. J. Int.*, *143*, 709–728, 2000.

Mooney, W., G. Laske, and G. Masters, A new global crustal model at 5 × 5 degrees: CRUST-5.1, *J. Geophys. Res.*, *103*, 727–747, 1998.

Navrotsky, A., Lower mantle phase transitions may generally have negative pressure-temperature slopes, *Geophys. Res. Lett.*, *7*, 709–711, 1980.

Neele, F., H. de Regt, and J. VanDecar, Gross errors in upper-mantle discontinuity topography from underside reflection data, *Geophys. J. Int.*, *129*, 194–204, 1997.

Niu, F., and H. Kawakatsu, Direct evidence for the undulation of the 660-km discontinuity beneath Tonga: Comparison of Japan and California array data, *Geophys. Res. Lett.*, *22*, 531–534, 1995.

Petersen, N., L. P. Vinnik, G. Kosarev, R. Kind, S. Oreshin, and K. Stammler, Sharpness of the mantle discontinuities, *Geophys. Res. Lett.*, *20*, 859–862, 1993.

Revenaugh, J., and T. H. Jordan, Mantle layering from *ScS* reverberation, 2. The transition zone, *J. Geophys. Res.*, *96*, 19,763–19,780, 1991.

Revenaugh, J. S., and S. A. Sipkin, Mantle discontinuity structure beneath China, *J. Geophys. Res.*, *99*, 21,911–21,927, 1994.

Richards, M. A., and C. W. Wicks, *S-P* conversion from the transition zone beneath Tonga and the nature of the 670 km discontinuity, *Geophys. J. Int.*, *101*, 1–35, 1990.

Ringwood, A. E., *Composition and Petrology of the Earth's Mantle*, 618 pp., McGraw-Hill, New York, 1975.

Ritsema, J., H. J. Van Heijst, and J. H. Woodhouse, Complex shear wave velocity structure imaged beneath Africa and Iceland, *Science*, *286*, 1925–1928, 1999.

Shearer, P. M., Seismic imaging of upper-mantle structure with new evidence for a 520-km discontinuity, *Nature*, *334*, 121–126, 1990.

Shearer, P. M., Global mapping of upper mantle reflectors from long-period *SS* precursors, *Geophys. J. Int.*, *115*, 878–904, 1993.

Shearer, P. M., Transition zone velocity gradients and the 520-km discontinuity, *J. Geophys. Res.*, *101*, 3053–3066, 1996.

Shearer, P. M., Upper mantle seismic discontinuities, in *Earth's Deep Interior: Mineral Physics and Tomography From the Atomic to the Global Scale, Geophys. Monogr. Ser.*, vol. 117, edited by S. Karato et al., pp. 115–131, AGU, Washington, D. C., 2000.

Shearer, P. M., and G. Masters, Global mapping of topography on the 660-km discontinuity, *Nature*, *355*, 791–796, 1992.

Shearer, P. M., M. P. Flanagan, and M. A. Hedlin, Experiments in migration processing of *SS* precursor data to image upper mantle discontinuity structure, *J. Geophys. Res.*, *104*, 7229–7242, 1999.

Shen, Y., S. C. Solomon, I. T. Bjarnason, and G. M. Purdy, Hot mantle transition zone beneath Iceland and the adjacent Mid-Atlantic Ridge inferred from *P*-to-*S* conversions and the 410- and 660-km discontinuities, *Geophys. Res. Lett.*, *23*, 3527–3530, 1996.

Shen, Y., A. F. Sheehan, K. G. Dueker, C. de Groot-Hedlin, and H. Gilbert, Mantle discontinuity structure beneath the southern East Pacific Rise from *P*-to-*S* converted phases, *Science*, *280*, 1232–1235, 1998.

Su, W.-J., R. L. Woodward, and A. M. Dziewonski, Degree-12 model of shear velocity heterogeneity in the mantle, *J. Geophys. Res.*, *99*, 6945–6980, 1994.

Thoraval, C., and P. Machetel, Accounting for phase changes and their kinetics within geodynamic model for the geoid, *Eos Trans. AGU*, *81*(46), Fall Meet. Suppl., Abstract T22E-07, 2000.

van der Lee, S., H. Paulssen, and G. Nolet, Variability of *P*660*s* phases as a consequence of topography of the 660 km discontinuity, *Phys. Earth Planet. Inter.*, *86*, 147–164, 1994.

Vidale, J. E., and H. M. Benz, Upper-mantle seismic discontinuities and the thermal structure of subduction zones, *Nature*, *356*, 678–683, 1992.

Vinnik, L. P., G. Kosarev, and N. Petersen, Mantle transition zone beneath Eurasia, *Geophys. Res. Lett.*, *23*, 1485–1488, 1996.

Wessel, P., and W. H. F. Smith, Free software helps map and display data, *Eos Trans. AGU*, *72*, 441, 445–446, 1991.

Wicks, C. W., and M. A. Richards, A detailed map of 660-kilometer discontinuity beneath the Izu-Bonin subduction zone, *Science*, *261*, 1424–1427, 1993.

Woodhouse, J. H., and A. M. Dziewonski, Mapping the upper mantle: Three-dimensional modeling of Earth structure by inversion of seismic waveforms, *J. Geophys. Res.*, *89*, 5953–5986, 1984.

Woodhouse, J. H., and A. M. Dziewonski, Seismic modeling of the Earth's large-scale three dimensional structure, *Philos. Trans. R. Soc. London*, *328*, 291–308, 1989.

Xu, F., J. E. Vidale, P. S. Earle, and H. M. Benz, Mantle discontinuities under southern Africa from precursors to $P'P'_{df}$, *Geophys. Res. Lett.*, *25*, 571–574, 1998.

Yamazaki, A., and K. Hirahara, The thickness of upper mantle discontinuities, as inferred from short-period J-Array data, *Geophys. Res. Lett.*, *21*, 1811–1814, 1994.

Yuen, D. A., D. M. Reuteler, S. Balachandar, V. Steinbach, A. V. Malevsky, and J. J. Smedsmo, Various influences on three-dimensional mantle convection with phase transitions, *Phys. Earth Planet. Inter.*, *86*, 185–203, 1994.

A. M. Dziewonski and Y. J. Gu, Department of Earth and Planetary Sciences, Harvard University, Cambridge, MA 02138, USA. (dziewons@seismology.harvard.edu; gu@seismology.harvard.edu)

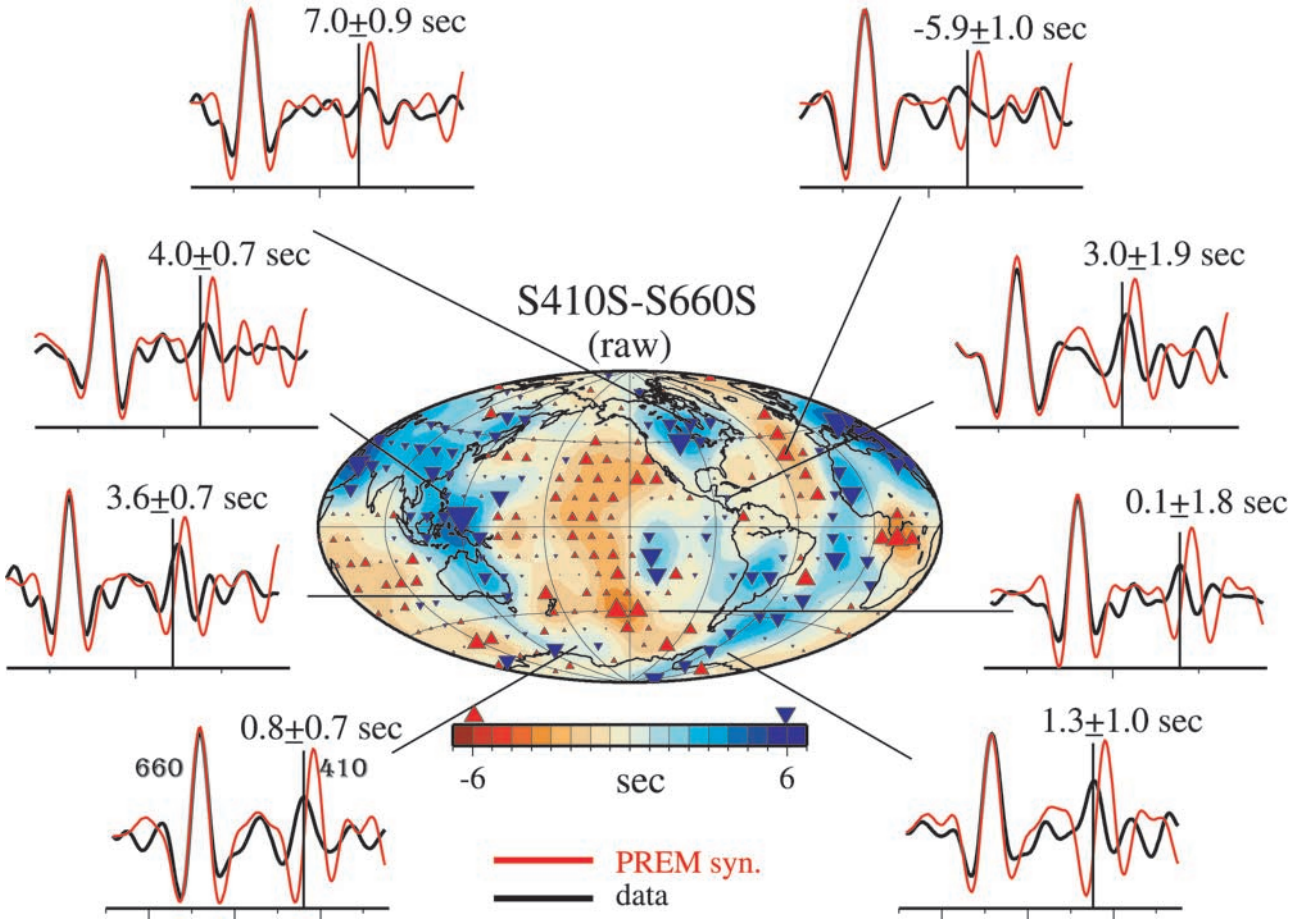

Figure 8. A global map of *S*410*S* – *S*660*S* without correcting for the velocity variations within the TZ. Red (or blue) triangles represent places where the TZ is thinner (or thicker) than the global average. The cap residuals are interpolated using a degree 12 spherical harmonic expansion. Sample stacks of synthetic and data autocorrelation functions are shown in red and black, respectively. The locations of the selected caps are indicated by the straight lines that connect the map locations with autocorrelation stacks. The *S*410*S* – *S*660*S* residuals are measured from the time shifts between the data and synthetic 410 correlation peak. The travel times reported here have removed the global average of −8.1 s (marked by the vertical line on each pair of autocorrelation stacks).

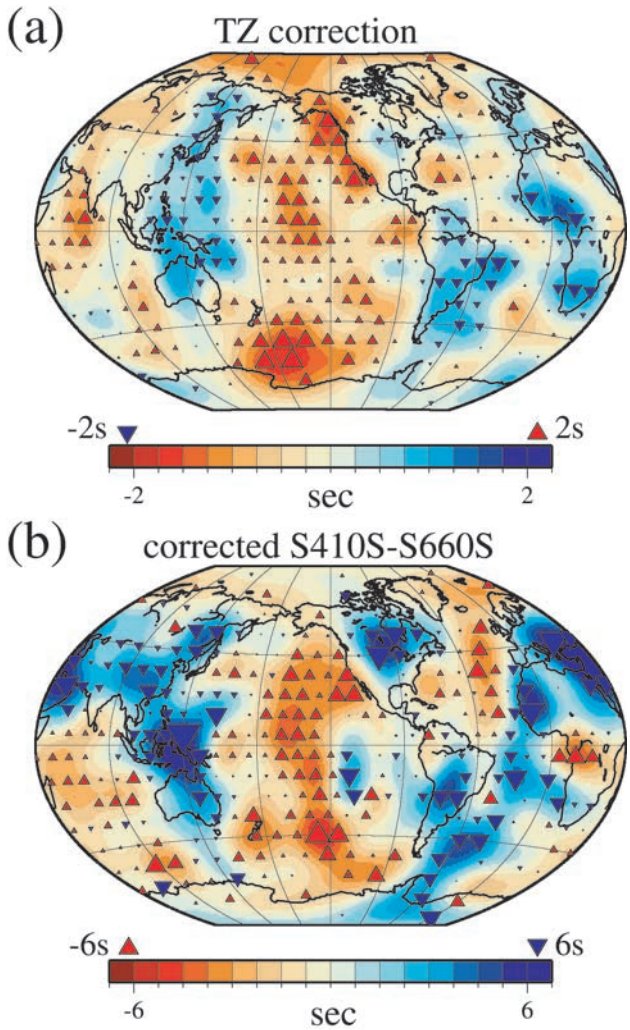

Figure 9. (a) Travel time corrections for the TZ structure, as predicted by S12/WM13 of *Su et al.* [1994]. The velocity perturbations at 550 km is plotted on the background. The triangles represent the correction values at the cap centers. Most corrections have absolute values of 2 s or less. (b) Residual of *S*410*S* – *S*660*S* after correcting for TZ velocity structure. The color conventions are the same as those of Figure 8. The range of *S*410*S* – *S*660*S* perturbations becomes slightly larger after the correction.

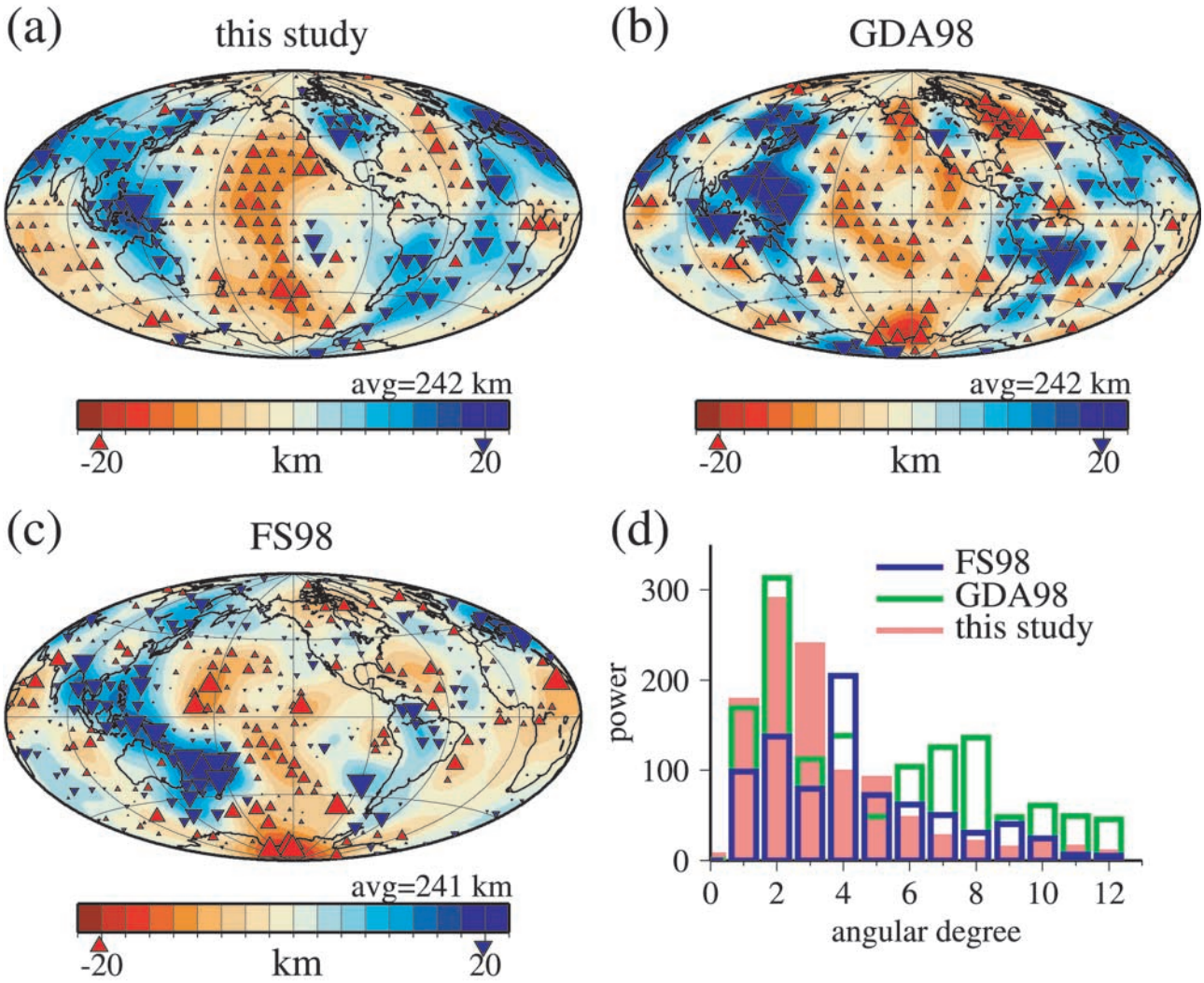

Figure 12. Thickness maps of the TZ. In each map, the residuals have been interpolated using a spherical harmonic expansion up to degree 12. The blue and red contours show the regions of thick and narrow TZ, respectively. (a) Thickness variations inferred from *S*410*S* – *S*660*S* residuals of this study. (b) Thickness variations in GDA98 inferred from *SS*–*SdS* residuals. (c) Thickness variations in FS98 inferred from *SS*–*SdS* residuals. Only caps with more than 20 records are shown. (d) Power spectra of all three thickness maps. The long-wavelength features are fairly consistent among these maps, as suggested by the agreement at the low-degree spherical harmonics.